SAND2016-2936R

Final report of Sandia National Laboratories (SNL) contribution to IAEA CRP F11016 on "Utilization of ion accelerators for studying and modeling of radiation induced defects in semiconductors and insulators"

György Vízkelethy
Sandia National Laboratories
Department of Ion-Solid Interactions
Albuquerque, NM 87185-1058, USA

Sandia National Laboratories is a multi-program laboratory managed and operated by Sandia Corporation, a wholly owned subsidiary of Lockheed Martin Corporation, for the U.S. Department of Energy's National Nuclear Security Administration under contract DE-AC04-94AL85000.

Introduction

This is the final report of Sandia National Laboratories' activities within the International Atomic Energy Agency (IAEA) Collaboration Research Project (CRP) F11016. The goal of this CRP is to study the effects of radiation on semiconductors and insulators with the emphasis on the effect of displacement damage due to MeV energy ions on the performance of semiconductor detectors and microelectronic devices. The devices used in this study were received from the university of Helsinki, but some other commercial diodes from Hamatsu were investigated, too. SNL's role in the project was to perform irradiation, C-V and Ion Beam Induced Charge (IBIC) measurements on the devices. In addition we performed Binary Collision Approximation (BCA) calculations to estimate the ionization and damage of the ions used in the experiment by the members of the CRP and created a TCAD model of the irradiation of the devices.

The SNL Ion Beam Laboratory (IBL)

The IBL is part of the Radiation Solid Interactions department (Org. 1111) at SNL. The IBL has several accelerators, a 100 kV focused ion beam system, a 350 kV HVEE accelerator, a 3 MV NEC single ended accelerator, and a 6 MV HVEE tandem accelerator that was used in this project. These accelerators are used in a variety of projects, among them for materials science, ion beam analysis (IBA), radiation effects, etc. The 100 kV focused ion beam system has a resolution of 10 nm and capable to produce heavy ions beams up to 200 keV. The 350 keV accelerator is mainly used to produce neutrons through the $D(d,n)^3He$ and $T(d,n)^4He$ reactions to calibrate detectors. The 3 MV NEC accelerator has several IBA beam lines, among them a high precision, high vacuum channeling chamber. This accelerator also has a microbeam line, which can focus protons and helium ions to a few hundred nm spot. The tandem accelerator is the most used equipment. In addition to some IBA beam lines (RBS, ERD) it has several beam lines that are dedicated to radiation effects. SNL has a large program to study displacement effects in electronics. In the past it was done using the Sandia Pulsed Reactor (SPR) that produced short neutron pulses. SPR was closed down in 2006 and SNL was searching for new ways to be able to study displacement effects. This effort led to the QASPR project that uses among others the IBL the simulate neutron displacement effects by using heavy ion beams. Two of the beam lines are dedicated to this project, QASPR III and QASPR II. QASPR III is used for everyday irradiations being able to irradiate as large as 4x4 mm^2 devices with ion beam pulses from < 1 μs to several hundreds of ms. In addition this beam line is equipped with 100 keV electron gun hitting the sample parallel to the ion beam. This beam line was used in some of the experiments performed for the CRP. The QASPR II beam line is similar to QASPR III, but it is less flexible in accommodating devices, but it is equipped with a cold stage and allows performing in-situ DLTS measurements. One beam line is dedicated to study microscopic mechanical changes

in solids due to irradiation. This beam line ends in a TEM chamber. A low energy Collutron accelerator beam is also injected in this chamber. This allows TEM studies of materials irradiated with two different ion beams.

The beam line that was mostly used for this project is the heavy ion microbe line. It can focus the ion beam to less than a μm and the beam can be scanned over a 200x200 μm^2 area (for light ions such as protons and He ions this area can be quite a bit larger). The chamber is equipped with a stage that can move reproducibly with 50 nm precision. The ion beam goes through an OM-40 optical microscope, so the irradiated area can be seen optically. The IBIC experiments were performed using a FastCOMTEC MPA-3 multi-parameter system where the ion hit location's x and y coordinated were recorded in coincidence with the IBIC signal.

SNL has its own version of the well-know BCA code Marlowe [1], that can handle crystal structures. The calculations were performed on the IBL's cluster that consists of several Dell workstations. In addition, using Silvaco's TCAD suite the IBIC process in the diodes were modeled.

Electrical characterization of the samples

The fabrication details of the samples are given in [2], so we will not go into details here. The device active area is 0.25 cm^2. On the p-type PINs the p+ layer is 3 μm and n+ layer in the back is 7 μm. On the n-type PINs both the p+ and n+ layers are 3 μm thick. The samples were packaged in 24-pin DIPs with connecting the front electrode to pin 3 and the back of the diode to pin 23. C-V measurements were performed using a Keithley 590 capacitance meter. At first we determined the stray capacitance due to the 24-pin DIP package, which we found to be 1.9 pF.

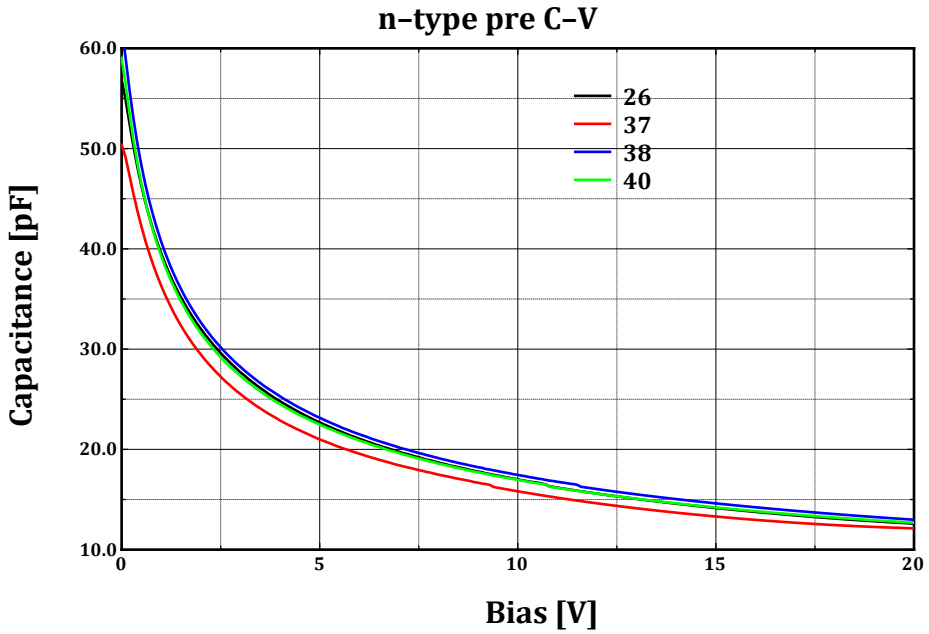

Figure 1 C-V curves of four n-type PINs

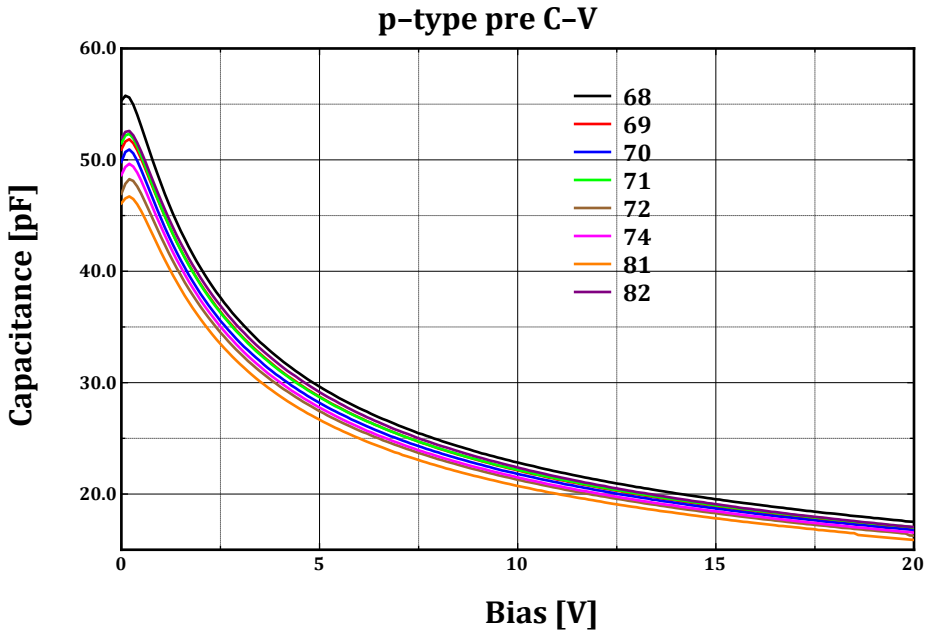

Figure 2 C-V curves of eight p-type PINs

Figure 1 and Figure 2 show the C-V curves for four n-type and eight p-type devices. There is some variation, but not significant. The peak in the C-V curves of the p-type devices at low bias voltages is still under discussion. Using these C-V curves and knowing the area of the diodes we can calculate the bias dependence of the depletion depth and the doping profile using equations (0.1) and (0.2)

$$W = \frac{\varepsilon_o \varepsilon_s A}{C} \tag{0.1}$$

$$N_d = \frac{2}{q\varepsilon_o \varepsilon_s A^2 \dfrac{d\left(1/C^2\right)}{dV}} \tag{0.2}$$

where N_d is the doping concentration, W is the depletion depth, C is the capacitance, A is the area of the diode, V is the bias voltage, ε_0 is the permittivity of the vacuum, and ε_s is the relative permittivity of silicon.

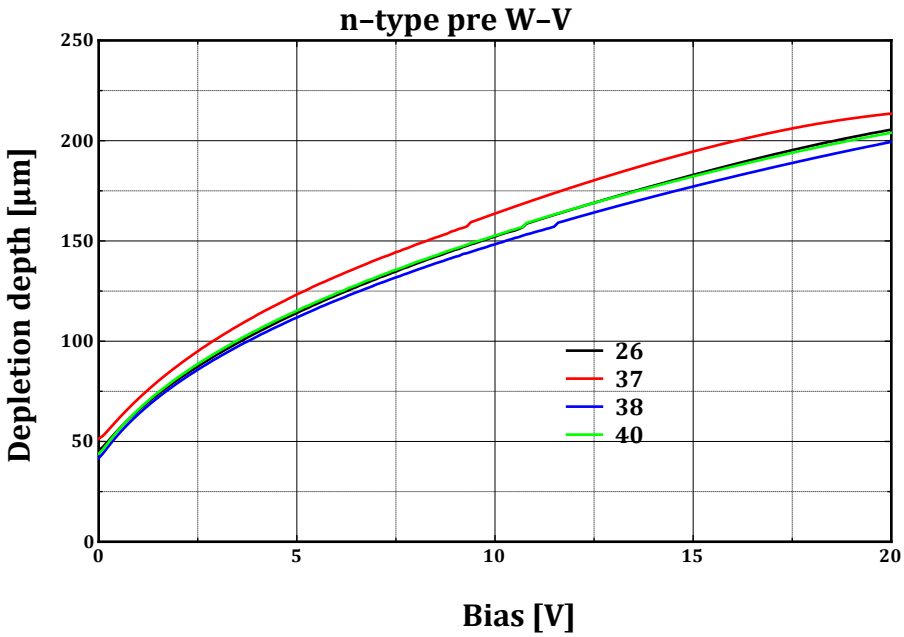

Figure 3 Bias dependence of the depletion depth of n-type PINs

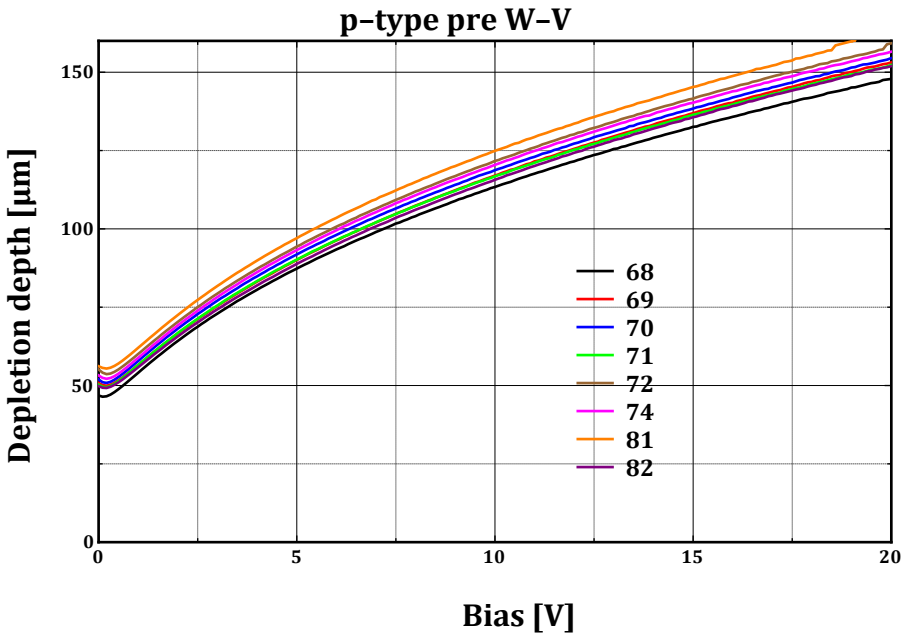

Figure 4 Bias dependence of the depletion depth of p-type PINs

Figure 3 and Figure 4 show the bias dependence of the depletion layer thickness of the devices up to 20 V. From the figures it is clear that both types of devices are already depleted to 50 µm at 0 V bias. The depletion depth at 20 V for the n-type devices is 200 µm while the depletion depth for the p-type devices is only 150 µm.

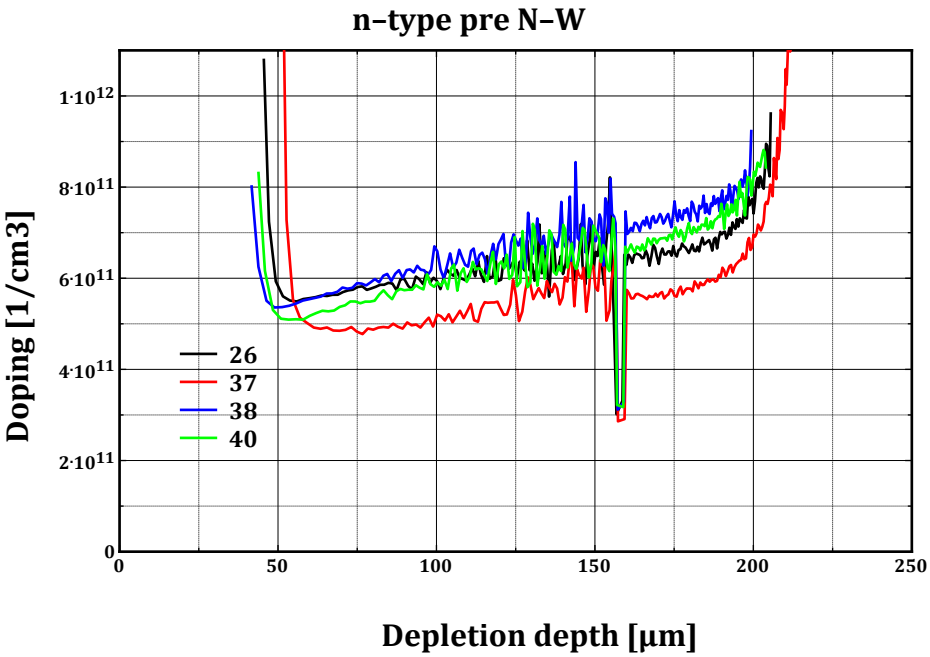

Figure 5 Doping level dependence on depth for n-type devices

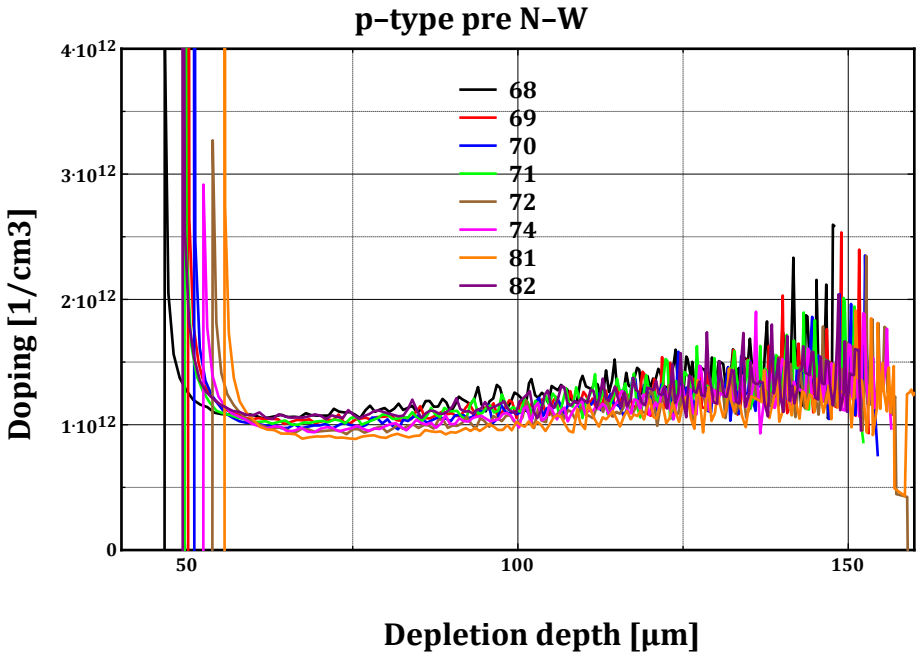

Figure 6 Doping level dependence on depth for p-type devices

Figure 5 and Figure 6 show the doping profiles calculated from the C-V measurements. The measurements give 5-6x10^{11} atoms/cm^3 for the n-type devices and 1x10^{12} atoms/cm^3 for the p-type devices, which agrees well with reference [2]. Since the devices did not seem to be fully depleted at 20 V (this is the maximum internal voltage of the Keithley 590), we performed C-V measurements up to 100 V on p81[1] and n26 devices using a Keithley 2400 external power supply. We used both auto range and fixed range of 200 pF. The reason for this measurement was the kink we saw in the C-V curves when the Keithley 590 switched range in auto range mode.

[1] The letter means the type of device (p or n) and the number is the serial number printed on the device.

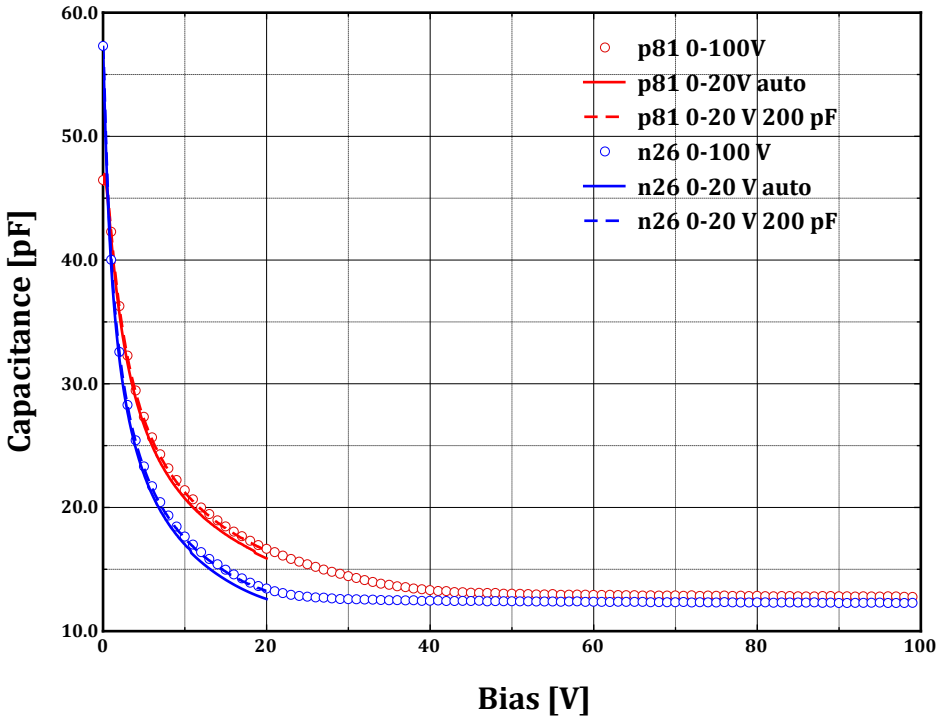

Figure 7 C-V curves up to 100 V and up to 20 V at auto range and fixed range

Figure 7 shows the C-V curves with fixed 200-pF range up to 100 V and at auto and fixed ranges up to 20 V. Although there is systematic difference between the auto and fixed range measurements, we consider the difference negligible.

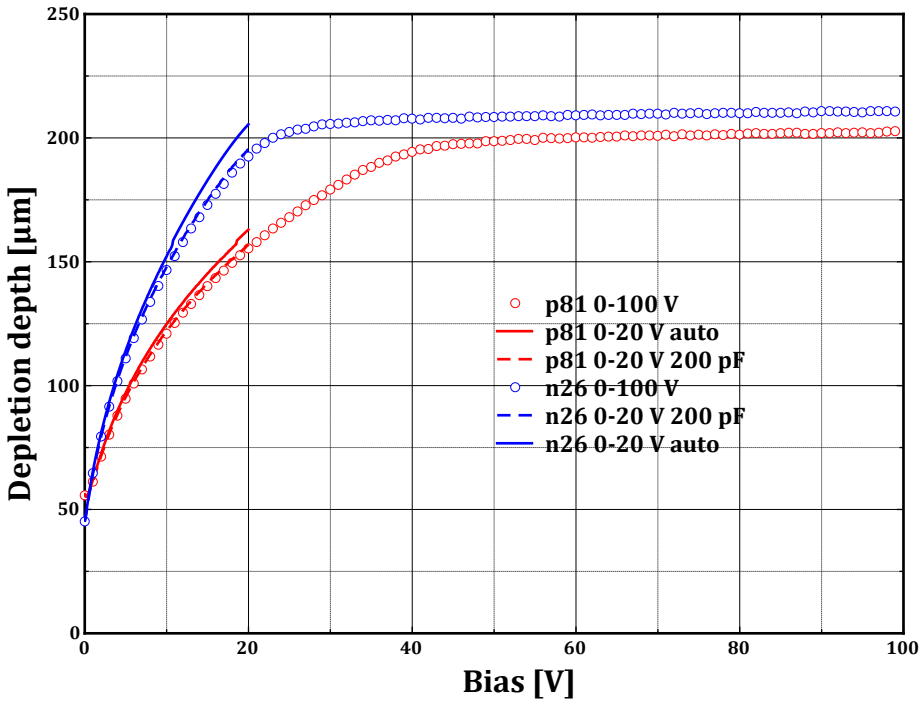

Figure 8 Depletion depth dependence on bias up to 100 V

Figure 8 shows the depletion depth dependence on applied bias. Again there is a slight difference between fixed and auto range measurements. The n-type devices reach saturation around 30 V with 210 µm depletion depth while the p-type devices reach the 200 µm maximum depletion depth at 50 V. These measurements indicate that in the future the C-V measurements should be done at least up to 50 V.

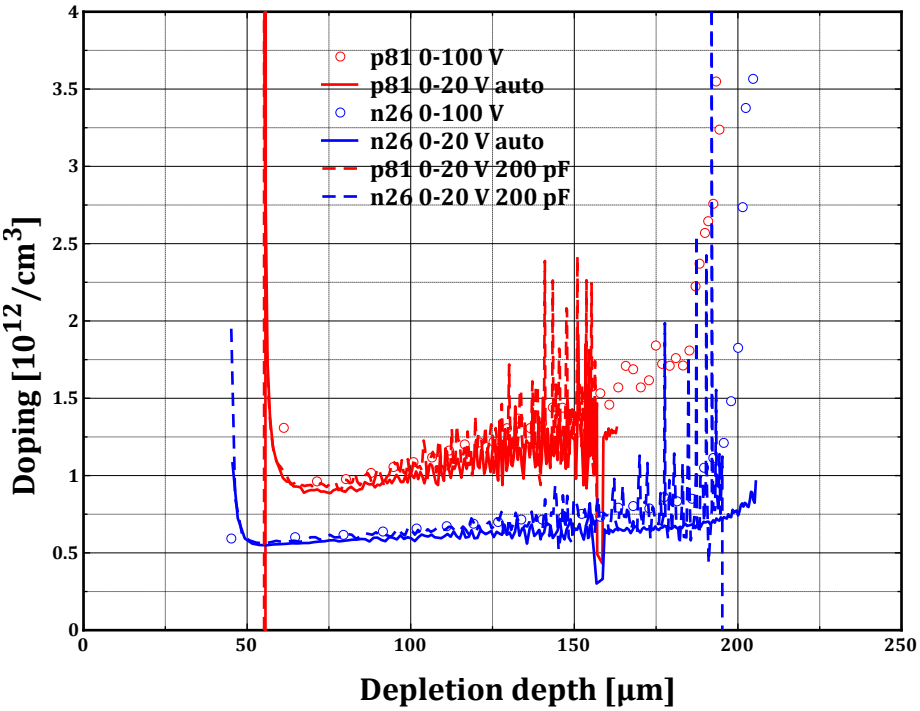

Figure 9 Doping level dependence on depth

Figure 9 shows the doping level dependence on the depth. This figure does not really provide more information than Figure 5 and Figure 6 this is only here for completness.

I-V measurements were performed using a Keithley 2400 source-meter.

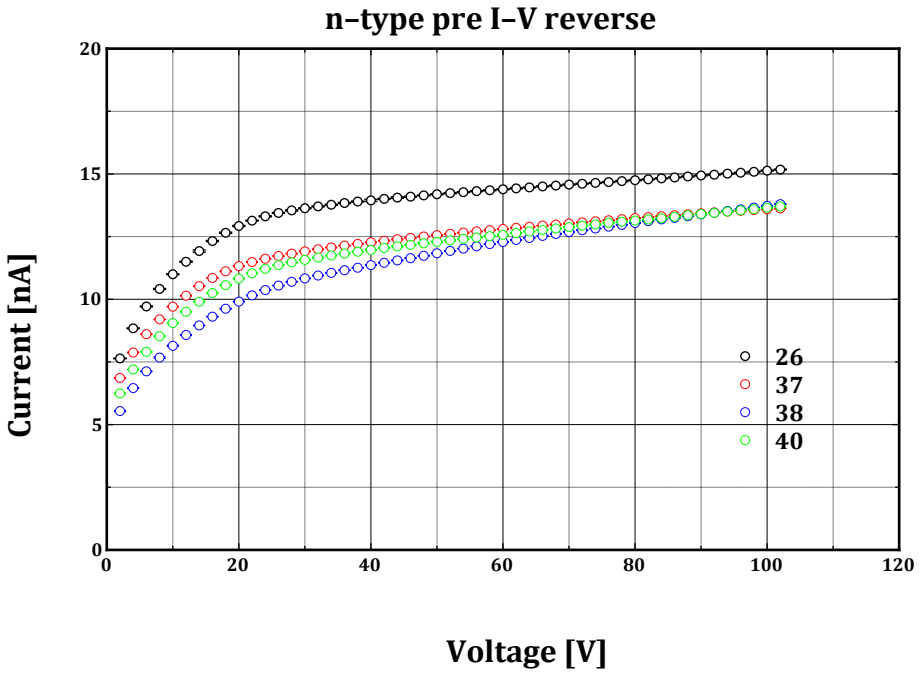

Figure 10 Leakage current vs. bias voltage for n-type PINs

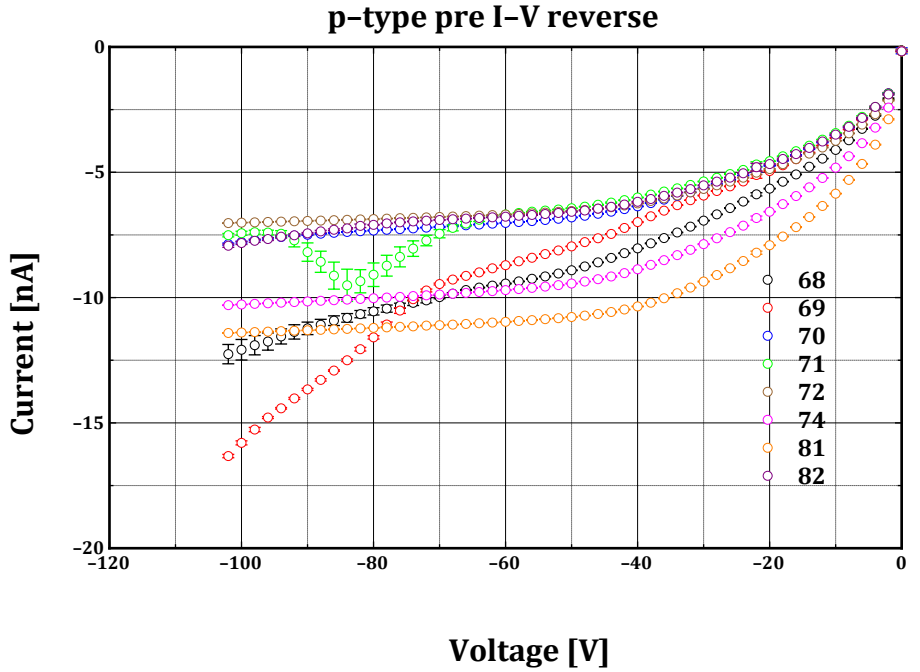

Figure 11 Leakage current vs. bias voltage for p-type PINs

Figure 10 and Figure 11 show the I-V curves for n and p-type devices in reverse bias mode. There are variations from device to device, but these variations are not significant. Generally we can say that the leakage current for undamaged devices is between 10-15 nA for the n-type devices and between 5-10 nA for the p-type devices. We also measured I-V curves in forward biased mode but we do not feel that this

data has any relevance to this project, so we decided to omit it in this report, the data are available on request.

Irradiation and in-situ monitoring of CCE degradation using the nuclear microbeam

Diodes p81 and n26 were selected to be irradiated with the SNL nuclear microprobe. The selected ions and energies were 4 and 8 MeV He and 4.5 MeV H based on previous discussion among the CRP members. The ion beams were focused to ~1x2 μm^2 spot and were rastered over a 100x100 μm^2 area. The irradiated spots were spaced apart by 200 µm to avoid overlap. The scan area was determined by an IBIC measurement on a 2000 mesh TEM grid mounted on a Hamamatsu S1223-01 PIN diode. Figure 12 shows the median map (on axis STIM image). The scan area and beam spot size were calculated fitting a line scan of the high-energy peak to the theoretical profile. Figure 13 shows the line profile in one direction with the fit. The inset shows the IBIC spectrum where the lower energy peak corresponds to the wires (green in Figure 12) and the higher energy peak corresponds to the holes (red in Figure 12) in the grid. The counts between the two peaks are due to the fact that the walls are not exactly vertical but slightly tapered. The scan area determination with this method gives an error of about 2%.

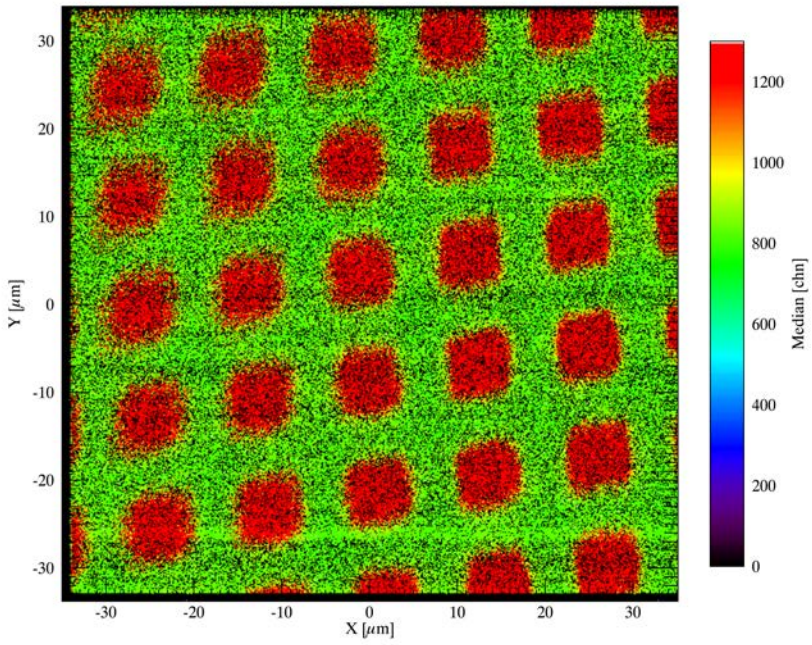

Figure 12 STIM image of a 2000 mesh TEM grid

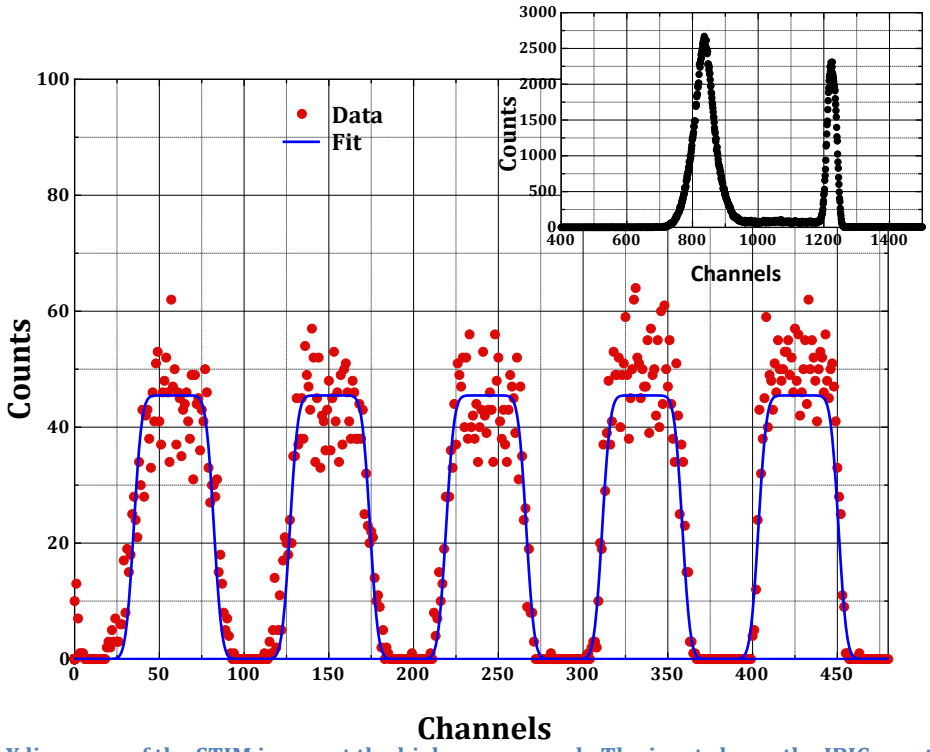

Figure 13 X line scan of the STIM image at the high-energy peak. The inset shows the IBIC spectrum

The spots were irradiated at about 1-2k ions/s rate. The fluence was measured through monitoring the IBIC signal using an Ortec 142A preamplifier and an Ortec 590A amplifier with a FastComtec Multiparameter data acquisition system. All irradiations were done at 0 V where the decrease in CCE is the most pronounced. Figure 14 shows the intensity distribution of one of the irradiated spots. The irradiation seems quite uniform. Note: This image is 512x512 pixels.

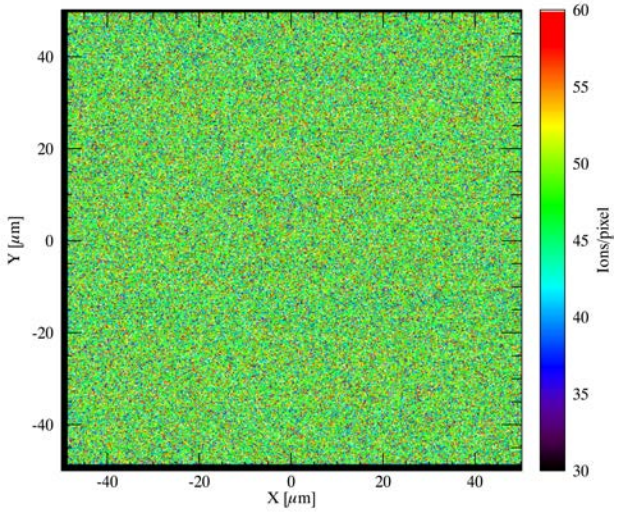

Figure 14 Intensity distribution of a sample irradiation

Even at this low count rate we had some pile-up as shown in Figure 15. To get a more precise fluence we calculated the pile-up rate (α) from the first 1000 counts where the pile-up peak and the normal peak did not overlap. Assuming that the pile-up rate is constant during the irradiation, the total number of ions is

$$N = N_0 \cdot \frac{1+2\cdot\alpha}{1+\alpha} \tag{0.3}$$

where N_0 is the total number of counts in the spectrum. The pile-up rate was never more than 3% and in most cases it stayed below 2%.

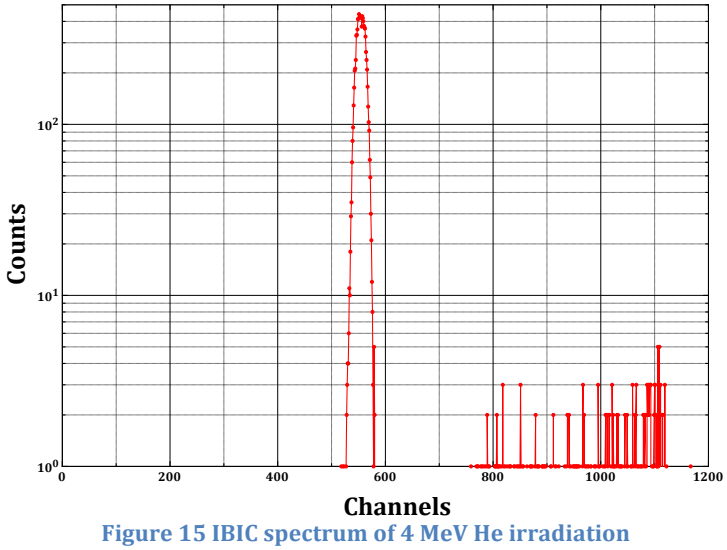

Figure 15 IBIC spectrum of 4 MeV He irradiation

Figure 17 - Figure 22 show the CCE degradation as the function of fluence measured by IBIC using the irradiation beam. The CCE degradation was calculated from a 50x50 μm^2 area around the center to avoid edge effects. The figures show the continuous CCE degradation for the largest fluence calculated for every 10k ions and the CCE degradation at the end of the irradiation for each individual spot. The fluence scale is logarithmic for each figure except for Figure 16. This figure has a linear fluence scale. From the figure it is easy to see that the CCE degradation becomes non-linear above 100 ions/μm^2 (10^{10} ions/cm^2) when the probing beam is the same as the irradiation beam.

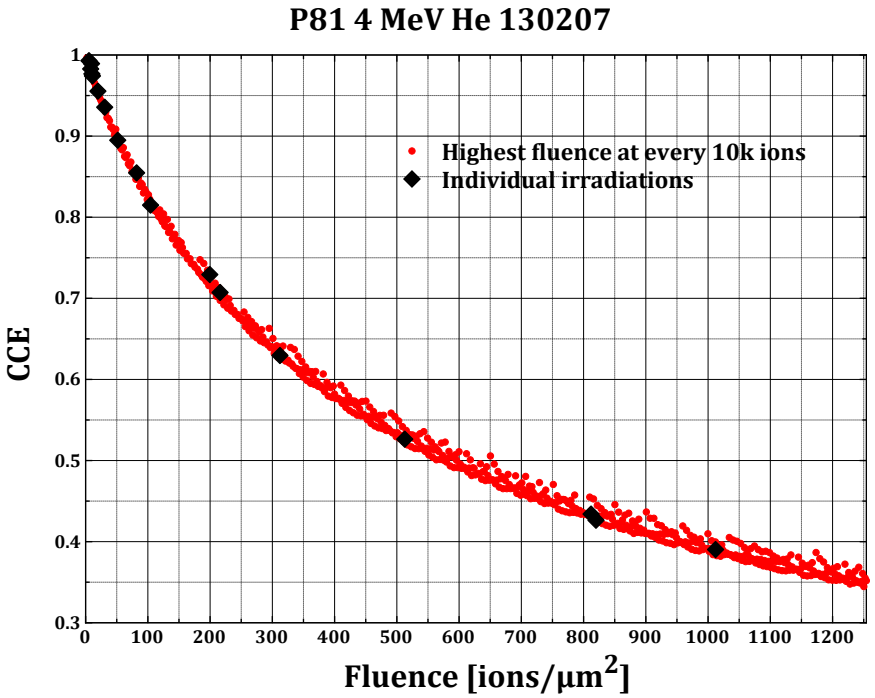

Figure 16 CCE degradation for 4 MeV He irradiation of p81 measured by the same He beam

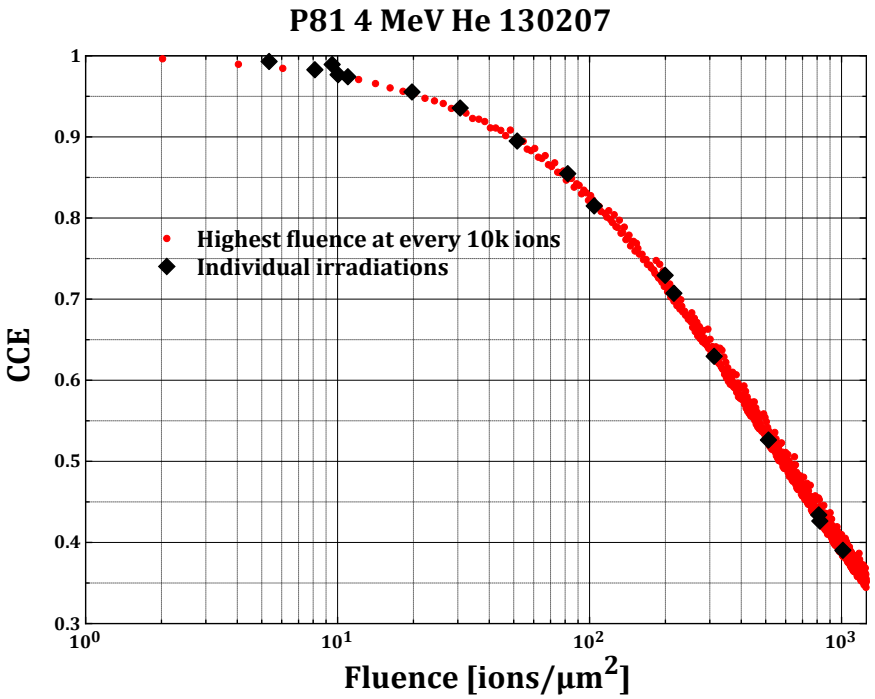

Figure 17 CCE degradation of 4 MeV He irradiation of p81 measured by the same He beam

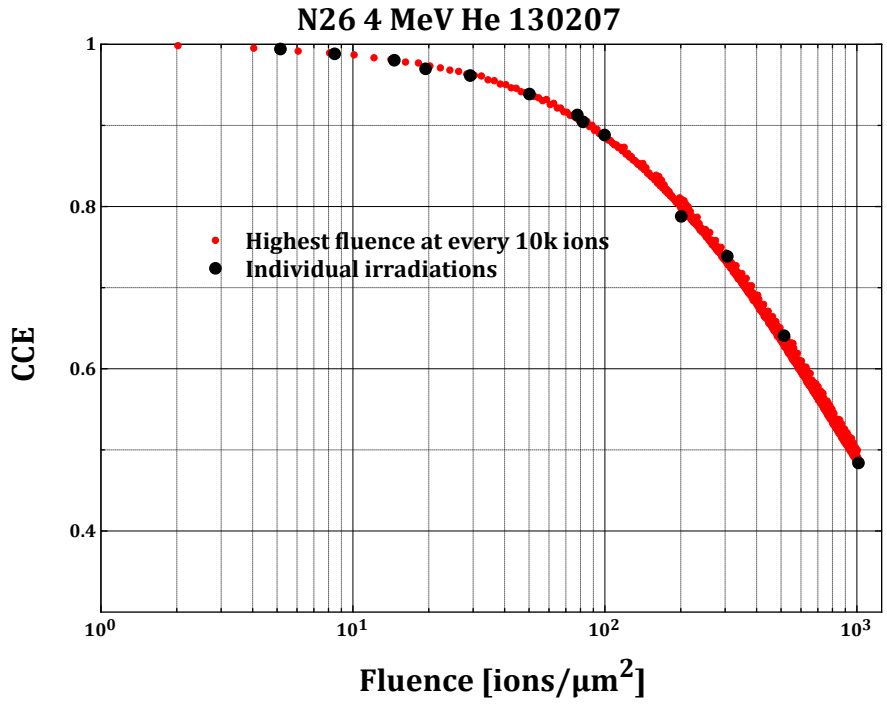

Figure 18 CCE degradation of 4 MeV irradiation of n26 measured by the same He beam

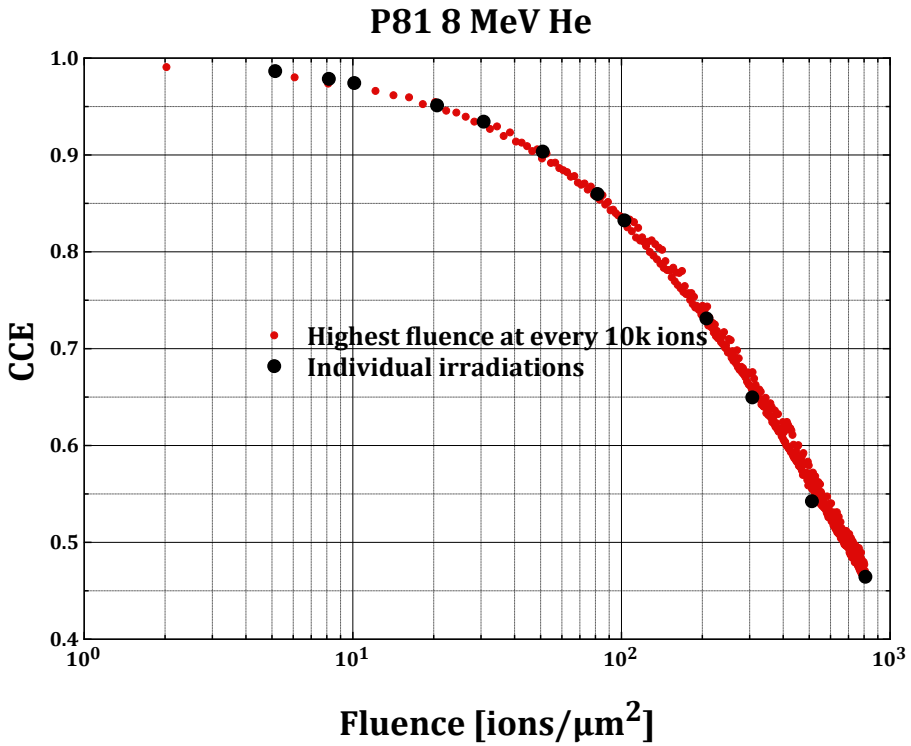

Figure 19 CCE degradation of 8 MeV irradiation of p81 measured by the same He beam

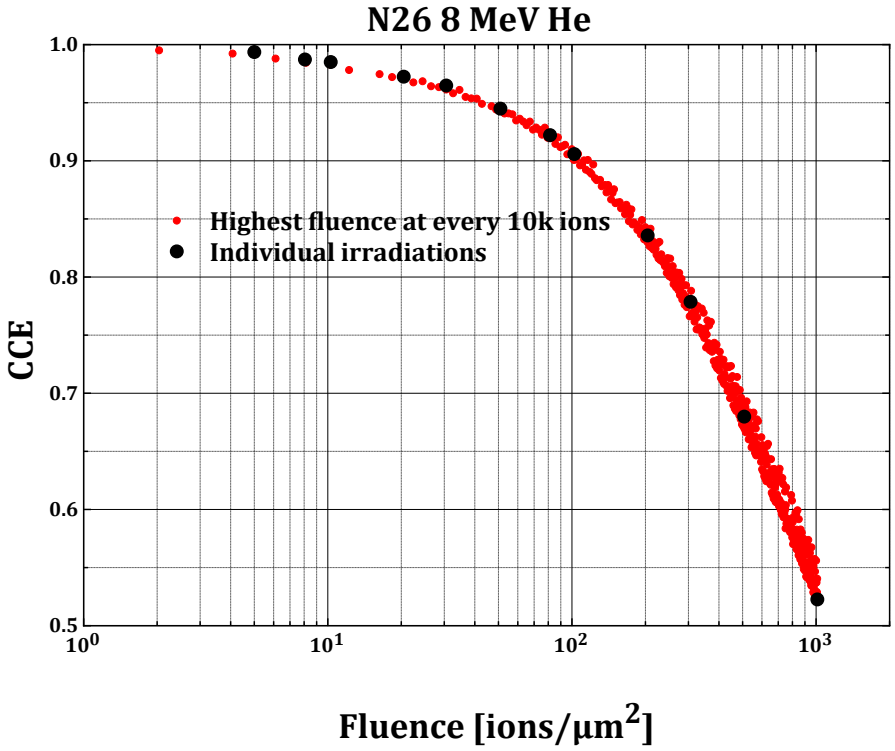

Figure 20 CCE degradation of 8 MeV irradiation of n26 measured by the same He beam

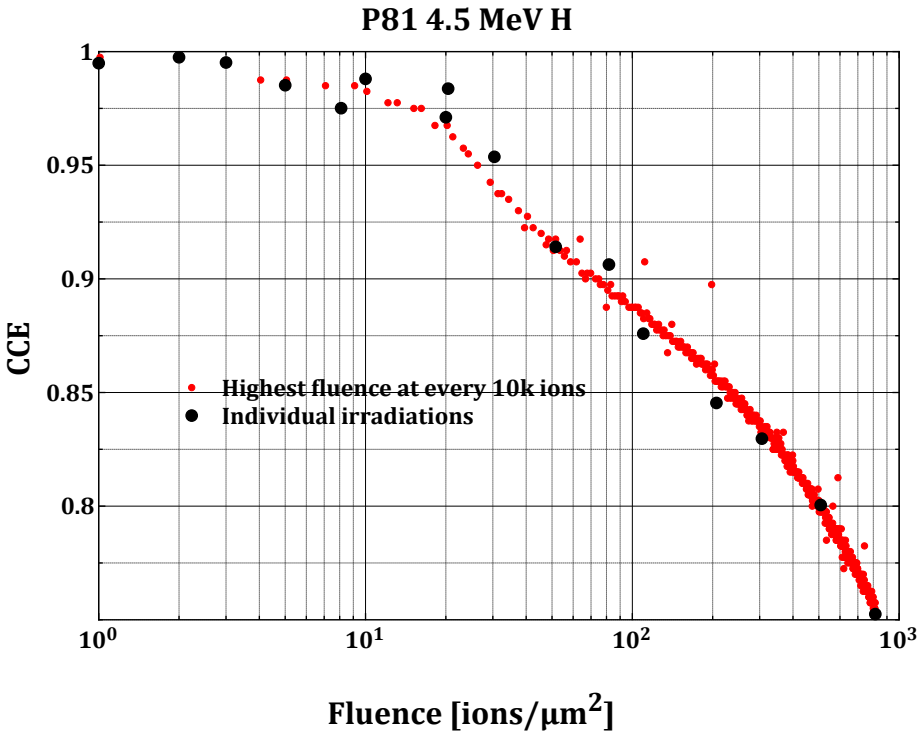

Figure 21 CCE degradation of 4.5 MeV H irradiation of p81 measured by the same H beam

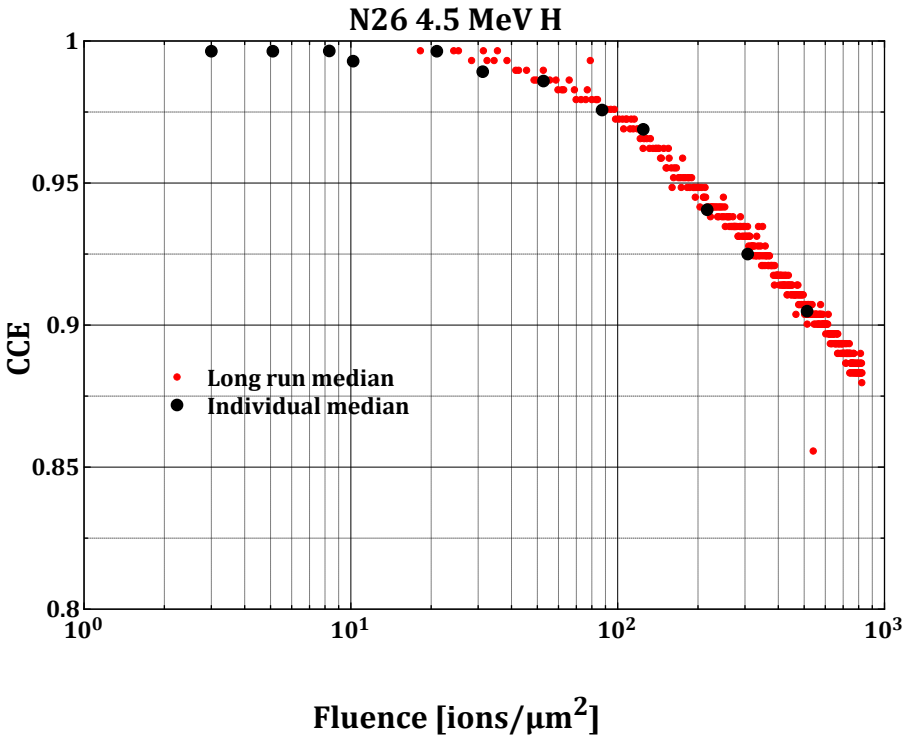

Figure 22 CCE degradation of 4.5 MeV H irradiation of n26 measured by the same H beam

IBIC characterization of the irradiated samples before and after ASTM annealing

All the irradiated parts were at a later time measured by 2 MeV He IBIC. At first we measured a bias curve for both parts on the un-irradiated areas. The CCE curves are shown in Figure 23. Both devices reach 100% CCE at around 30 V.

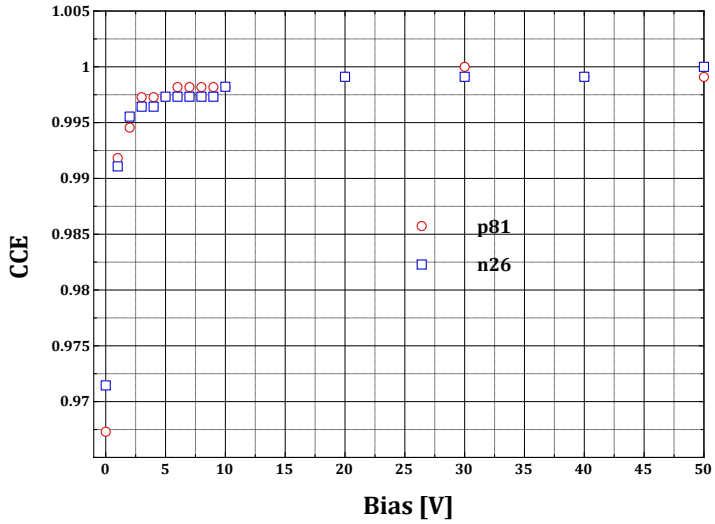

Figure 23 Bias curves of undamaged diodes with 2 MeV He

Since our microprobe cannot scan more than a few hundred μm, we could not scan all the irradiated spots at the same time. During the irradiation we recorded the coordinates of the center of each spot and a reference mark using our Escosy navigation system, which nominally has 50 nm positioning precision. Even with this the absolute coordinates were not very useful since the sample holder and the devices were taken out and put back in the chamber. We used the relative coordinates of the spot with the highest fluence, moved there, measured an IBIC map at 0 V bias and centered the beam scan over the spot. Then we moved to the other spots using the relative distances. We scanned over a 200x200 μm^2 area and selected a 50x50 μm^2 area in the center to determine the IBIC signal in the damaged spot, and a 25x25 μm^2 in the upper right corner of the scan to determine the undamaged IBIC signal. This way we could compensate for the spatial variation of the signal from the undamaged diode. Figure 24 shows the IBIC median map at the 4 MeV highest irradiation fluence of n26. The image clearly shows the 100x100 μm^2 irradiation (the shape is square) and the circular region, which is due to carriers diffusing into the damaged region. It also shows that carriers created close to the edge of the scan produce full CCE. The two white squares indicate the regions where the damaged and undamaged IBIC signals are calculated.

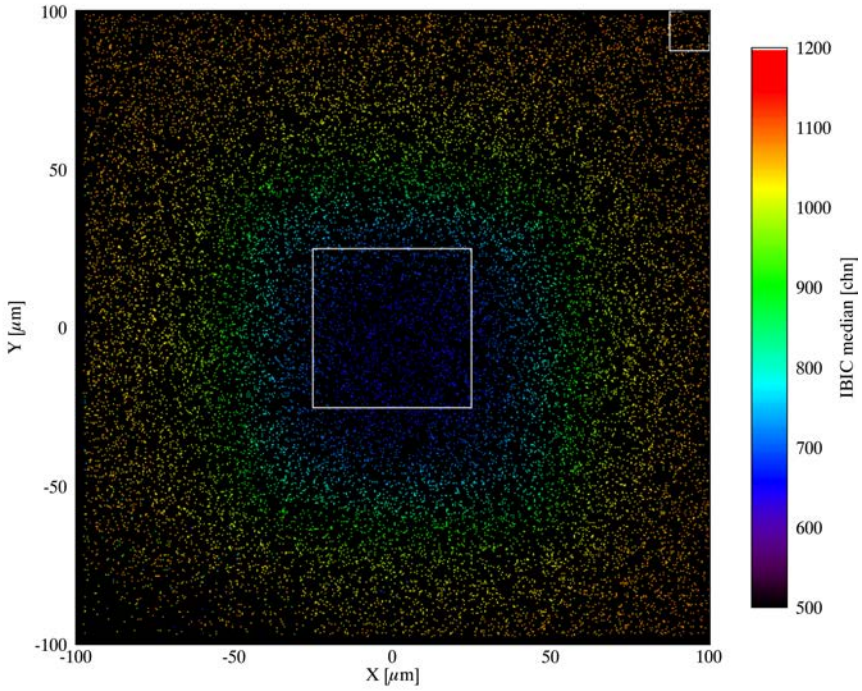

Figure 24 IBIC median map of 4 MeV He irradiated n26

The IBIC signals were calculated at 0, 10, and 50 V bias voltages and the CCE was calculated. Figure 25 – Figure 30 show the CCE degradation as the function of irradiation fluence measured with the 2 MeV He beam. The inset in each figure has a

linear fluence axis. Except for the 4 MeV irradiation of p81 the CCE vs. fluence curves seem to be linear; therefore, the model can be applied.

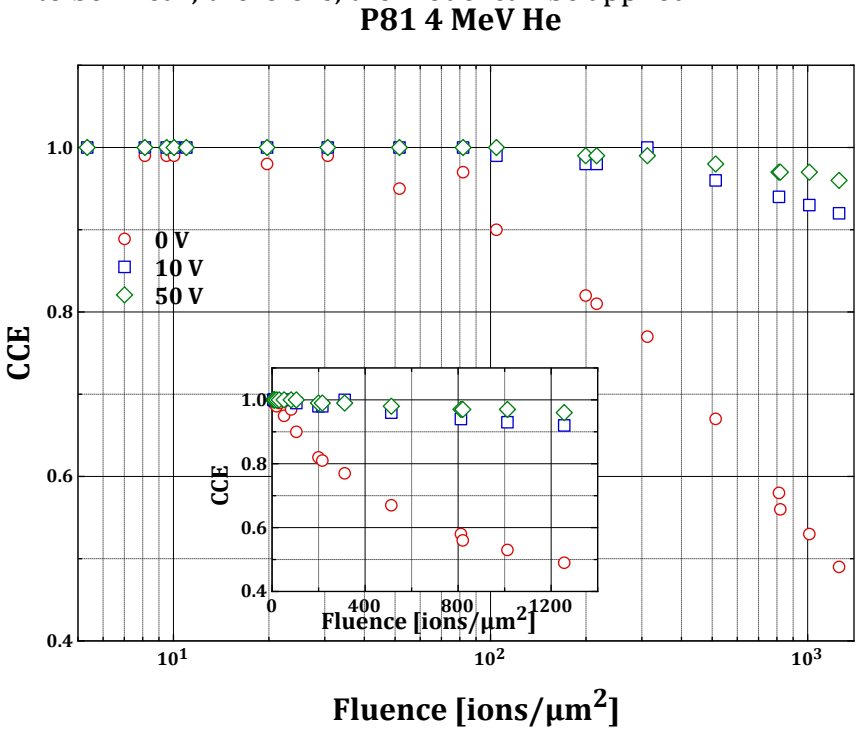

Figure 25 CCE of 2 MeV He of 4 MeV He irradiated p81

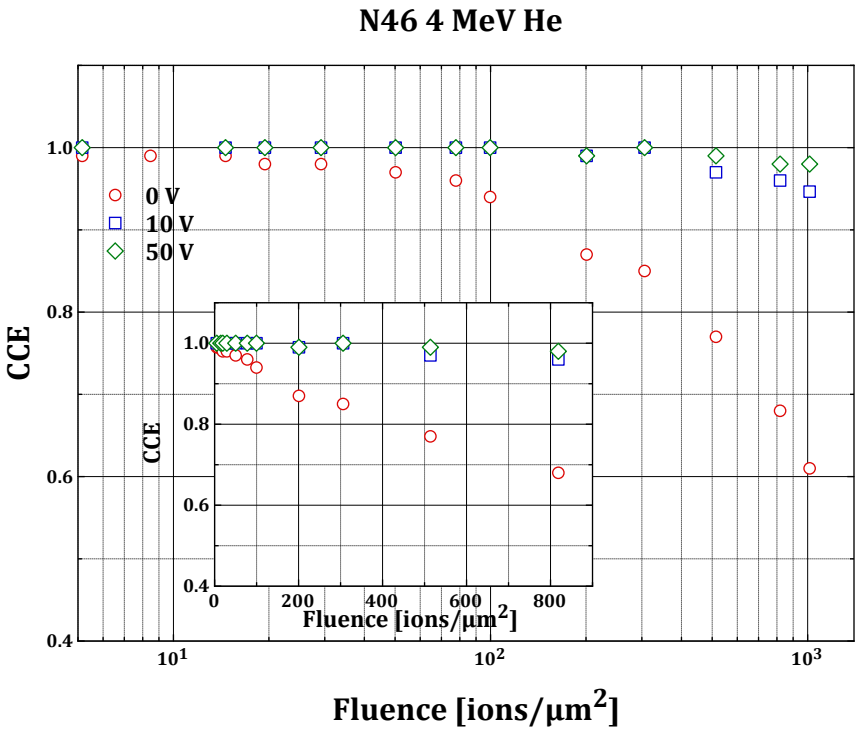

Figure 26 CCE of 2 MeV He of 4 MeV He irradiated n26

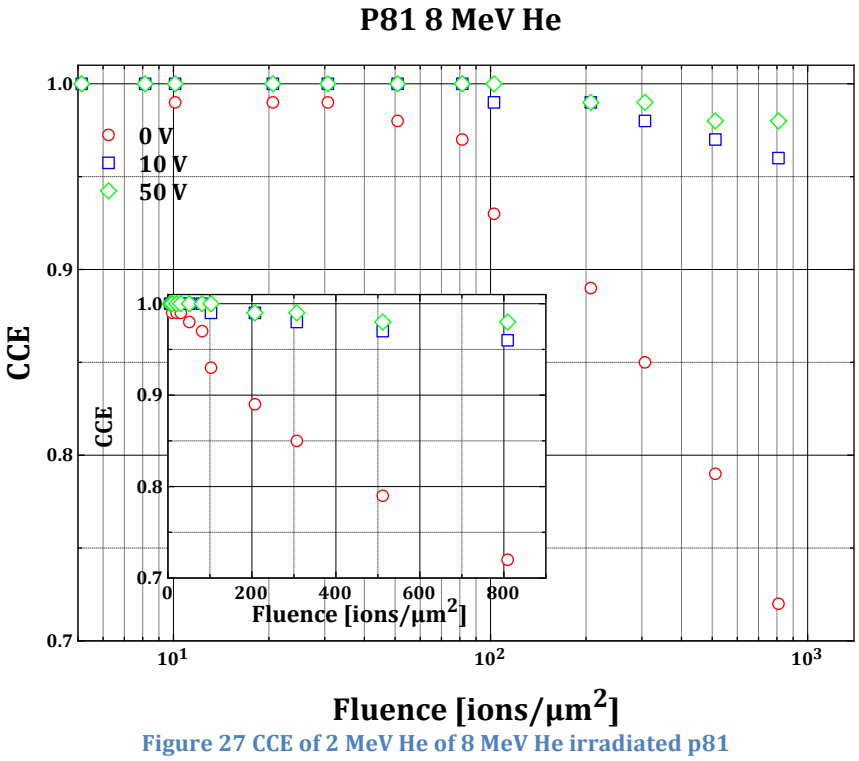

Figure 27 CCE of 2 MeV He of 8 MeV He irradiated p81

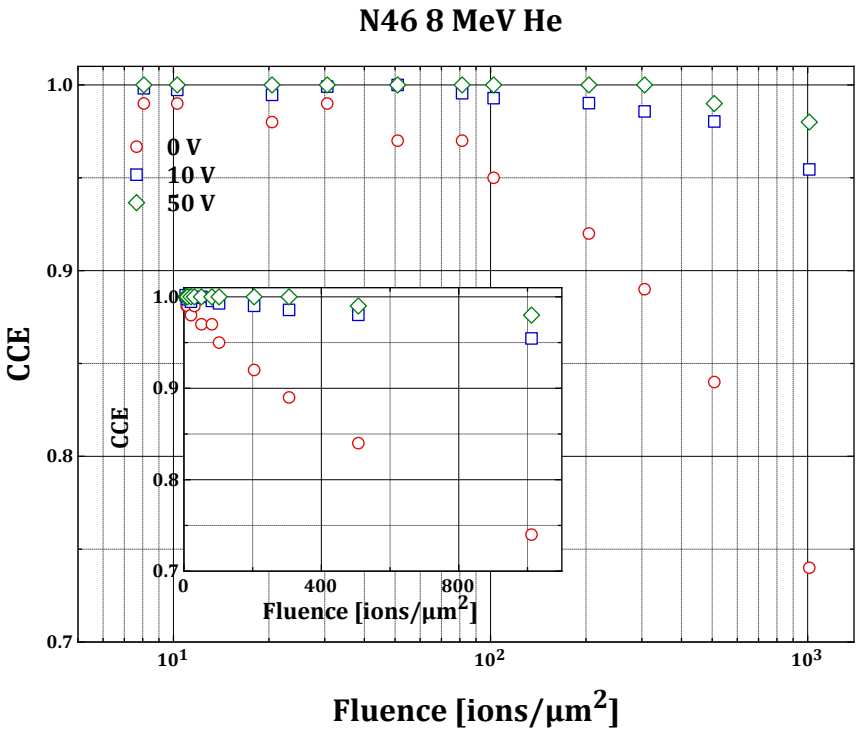

Figure 28 CCE of 2 MeV He of 8 MeV He irradiated n26

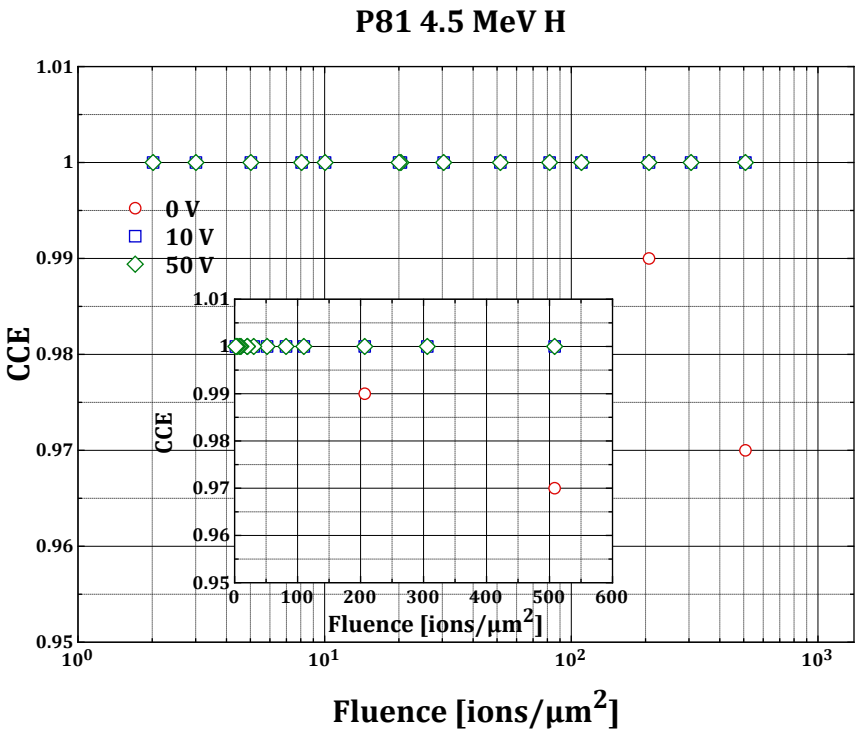

Figure 29 CCE of 2 MeV He of 4.5 MeV H irradiated p81

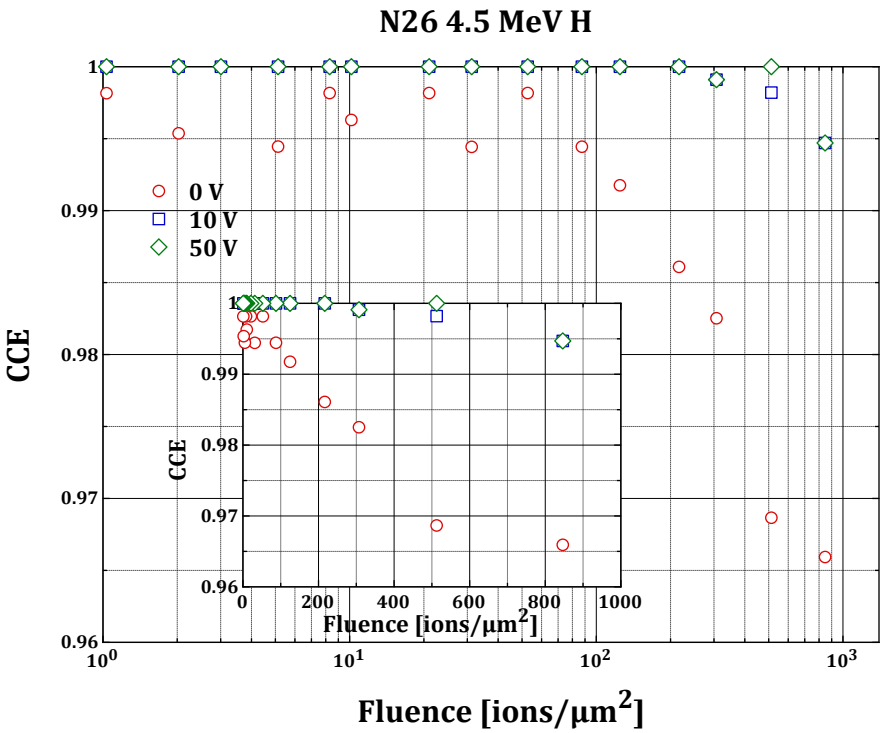

Figure 30 CCE of 2 MeV He of 4.5 MeV H irradiated n26

After the 2 MeV He IBIC measurements the devices were annealed at 80°C for two hours in air as prescribed by [3]. This annealing is supposed to remove all the transient defects and leave only the permanent defects. The new CCE vs. fluence curves show the same general features in most cases, the CCE is somewhat higher than be-

fore annealing. This change is small and in most cases the curves overlap within error. Figure 31 shows the case when the difference is the largest between the before and after annealing curves. We do not think that the difference is large enough not to use the before annealing curves. The difference is expected to be small since the samples were measured for the first time ten days after the irradiation.

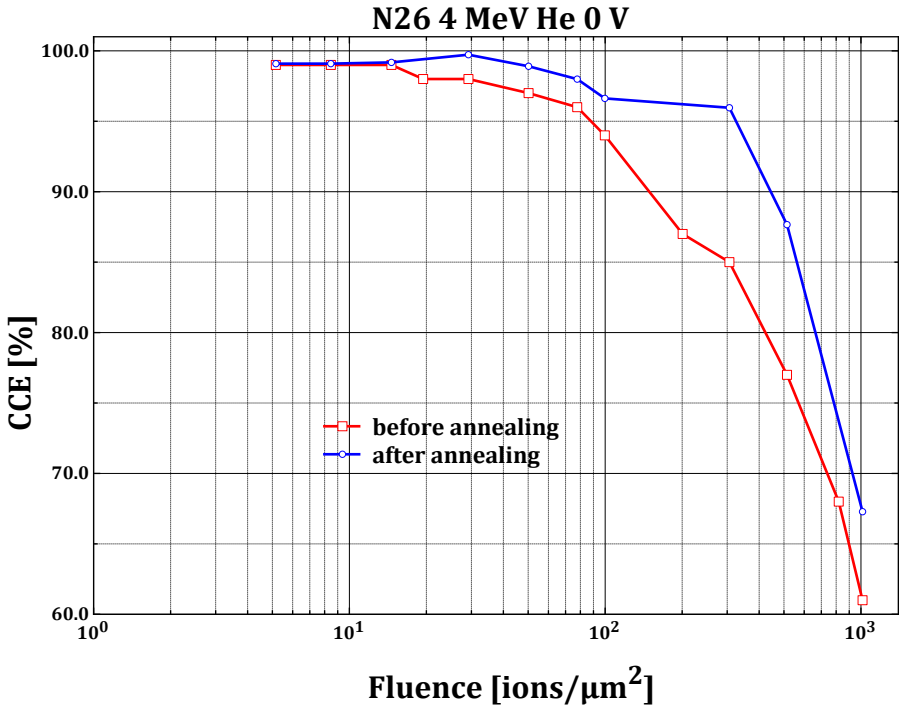

Figure 31 2 MeV IBIC of 4 MeV He irradiated n26 at 0 V before and after annealing

Electron irradiation

Two diodes, n27 and p1, were irradiated with 1 MeV electrons at 10^{15} electrons/cm^2 fluence at the Takasaki facility of JAEA. Then the diodes were shipped to SNL where they were characterized by C-V, I-V, and IBIC measurements. Since we could not measure these devices before irradiation, here we compare them to similar un-irradiated devices. Figure 32 and Figure 33 show the C-V curves for the electron irradiated and three un-irradiated devices. The un-irradiated devices have a very small spread; therefore, we believe that we can use them as un-irradiated standards for the electron irradiated devices. In both cases the capacitance at 0 V decreased significantly, it dropped from ~ 60 pF to 30 pF (p-type) and 20 pF (n-type). Also, both devices show a peak at low voltages similar that the virgin p-type device showed but to a much larger extent. This phenomenon needs more consideration and an explanation is not available at this time. Since there is a passivation layer on the diodes we speculate the decrease in 0 V capacitance is mainly due to charge trapped in this passivation layer.

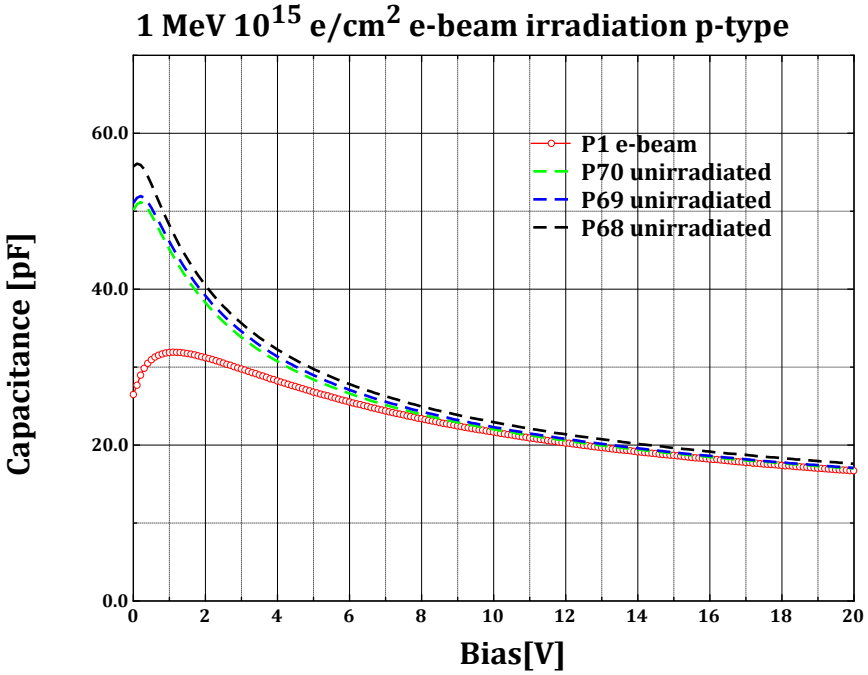

Figure 32 C-V curves of p-type un-irradiated and electron beam irradiated diodes

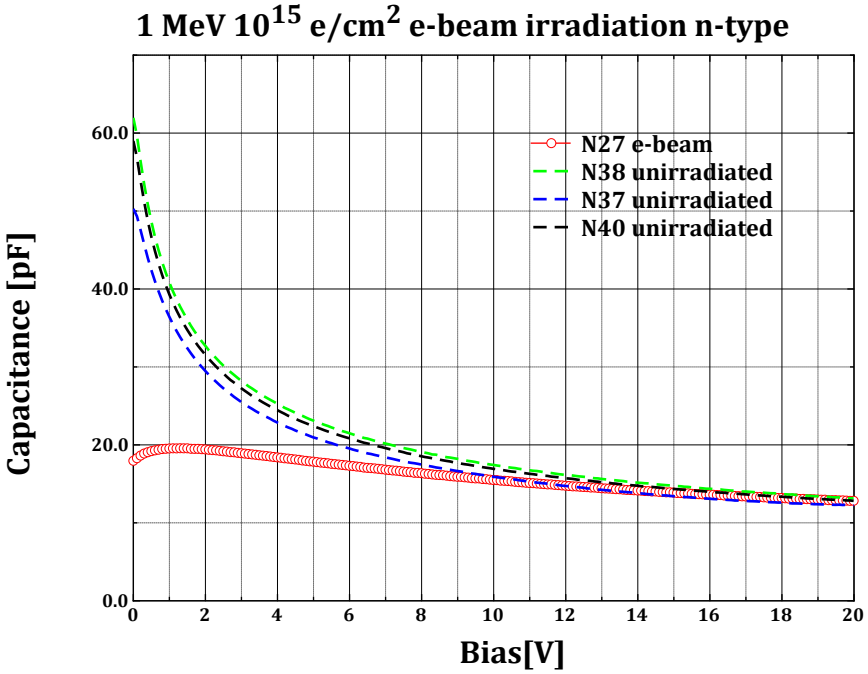

Figure 33 C-V curves of n-type un-irradiated and electron beam irradiated diodes

Using equation (0.2) we can calculate the apparent doping profiles. Due to the trapped charge in the passivation layer the devices are further depleted at 0 V than the 50 μm we observed for un-irradiated devices, ~ 80 μm for the p-type and 130 μm for the n-type diode. Figure 34 and Figure 35 show the apparent doping profile dependence on the depth. Both devices show excess charge according to their type, negative charge in the p-type and positive charge in the n-type diode. These results need further work to correctly interpret them.

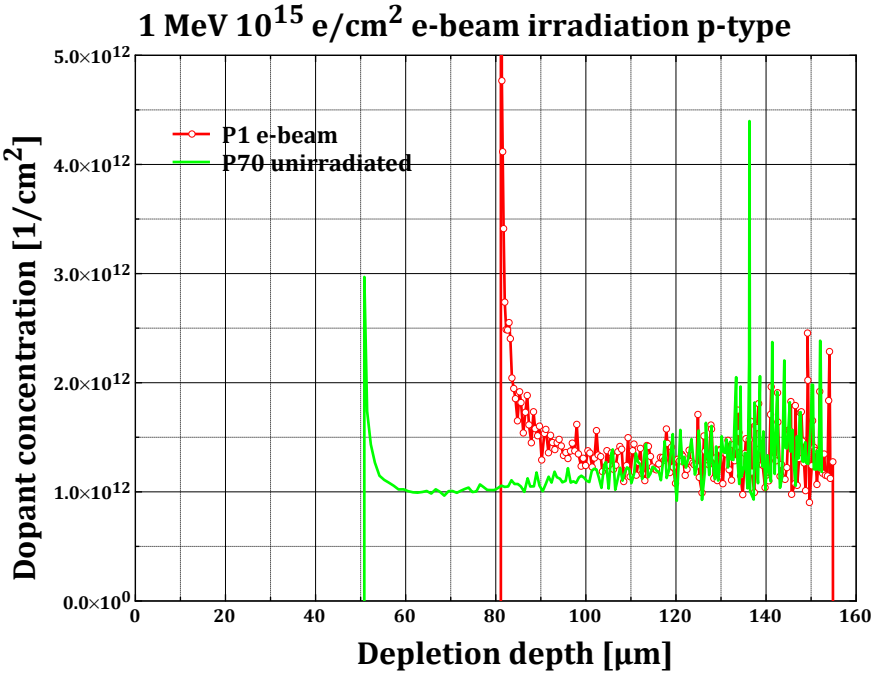

Figure 34 Apparent doping vs. depth for p1

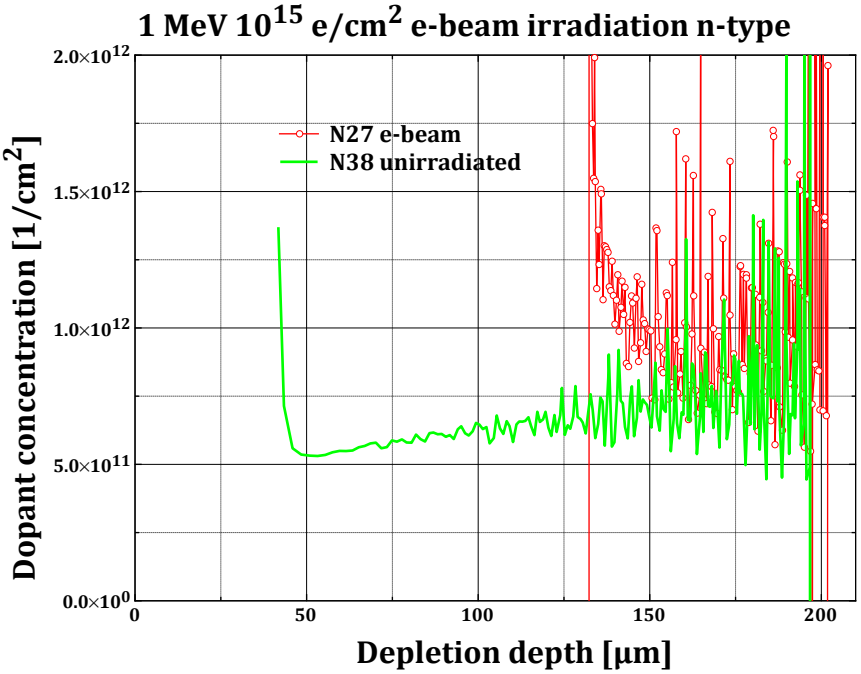

Figure 35 Apparent doping vs. depth for n27

We also measured I-V curves for the electron-irradiated diodes. In both diodes the leakage current went up by two orders of magnitude, from ~ 10 nA to a few µA.

Bias curves for both types of diodes were measured. Unfortunately, we had no opportunity to measure the bias curves before irradiation, so we cannot make a valid comparison. The saturation values of the IBIC signals were actually larger than for the un-irradiated p81 and n26 diodes. Also, during the measurement we realized

that due to the large leakage current the actual bias was not the one we set on the power supply. The Ortec 142A has a 100 MΩ bias resistor to protect detectors from overvoltage. With a few nA of leakage current it makes no difference but at μA currents almost all the voltage drops over the bias resistor. Therefore, we used the I-V curves we measured and calculated the actual bias voltage that was applied. We remeasured p1 a week later and found quite a bit of discrepancy with the previous measurement. A consequent measurement gave the same result. We have no explanation for the discrepancy between the two measurements one week apart. Figure 36 shows the bias curves with the corrected bias. The n and p-type devices are quite different. While the n-type diode seems to reach saturation around 10 V the IBIC signal of the p-type device seem increasing and slowly leveling above 40 V. If we consider p81 and n26 as the undamaged IBIC signal at 0 V, then the CCE degradation of p1 and n27 is about 88% and 81%, respectively[2].

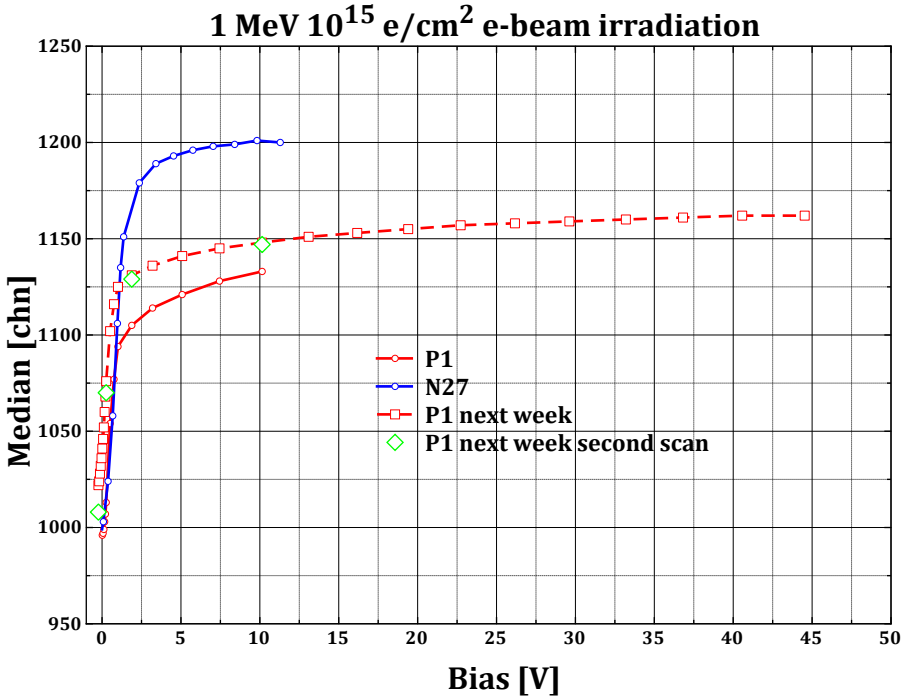

Figure 36 Bias curves for electron irradiated devices

Full area irradiations

Since in the microbeam irradiated devices the damage is negligible compared to the whole volume of the device, the C-V and I-V measurements do not offer any new information. The C-V measurements after the irradiation gave practically the same results as before. In order to see how the ion beam irradiation affects the bulk proper-

[2] This assumption does not seem to be justified very well in light of the fact that the IBIC signals for both p1 and n27 at around saturation are significantly larger than at the same voltages for p81 and n26.

ties of these devices we irradiated three devices of each type with 4 and 8 MeV He at ~ 10^{10} ions/cm^2 and 4.5 MeV H at ~ 1.2x10^{12} ions/cm^2. We aimed to get a CCE change around 10% where we hoped to see a change in the C-V curves. We were trying to extrapolate in case of the H beam and ended up with a too high fluence that caused significantly larger damage than intended. The devices were irradiated using the SNL pulsed irradiation facility [4]. These diodes are so large that even this system cannot irradiate the devices with one pulse; we had to use several pulses while we moved the devices. Although the individual pulses had fluences within 1%, due to the poor uniformity of the beam spots the irradiations were anything but uniform. The average fluences are correct but we have no information on the spatial variations. Therefore, we should consider the results as qualitative and not quantitative. The leakage currents increased by about 1.5 orders of magnitude for the He irradiations and by about three orders of magnitude for the H irradiations. In case of the 4 MeV He irradiations the C-V curves changed very little; therefore, we omit them here. Figure 37 and Figure 38 show the pre and post irradiation C-V curves for the 8 MeV He irradiated devices. In both cases there is slight decrease in capacitance. The corresponding doping profile vs. depth curves are shown in Figure 39 and Figure 40. The doping profiles show opposite behavior in the p and n-type devices. In the p-type devices the apparent doping level increased while in the n-type it decreased. This indicates extra negative charge in both cases. The correct interpretation of these results is pending.

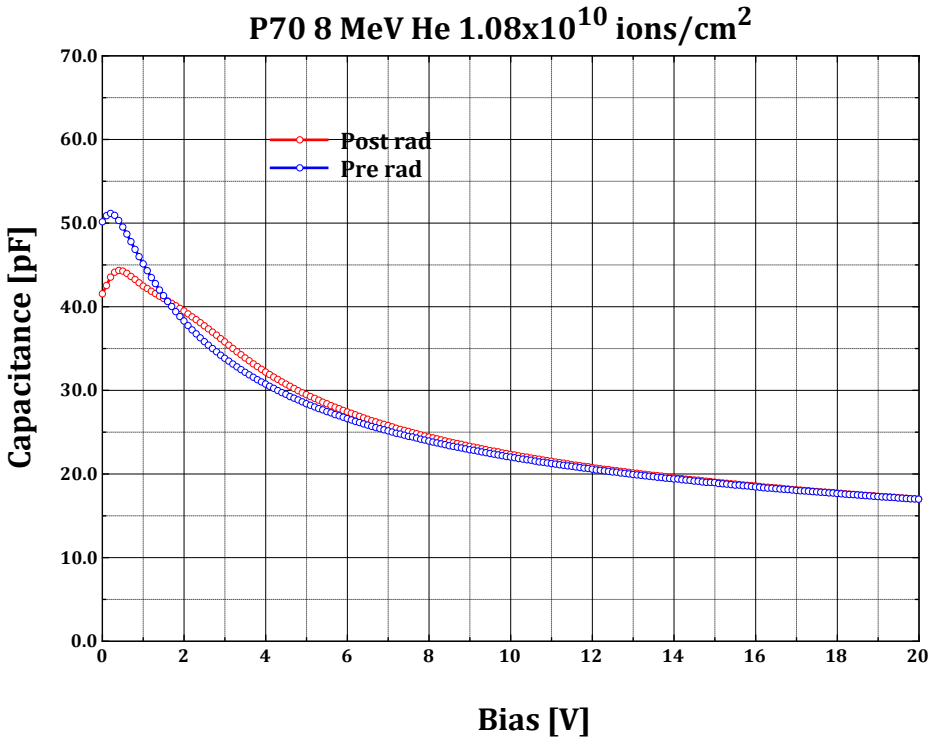

Figure 37 Pre and post irradiation C-V curves 8 MeV He irradiated p70

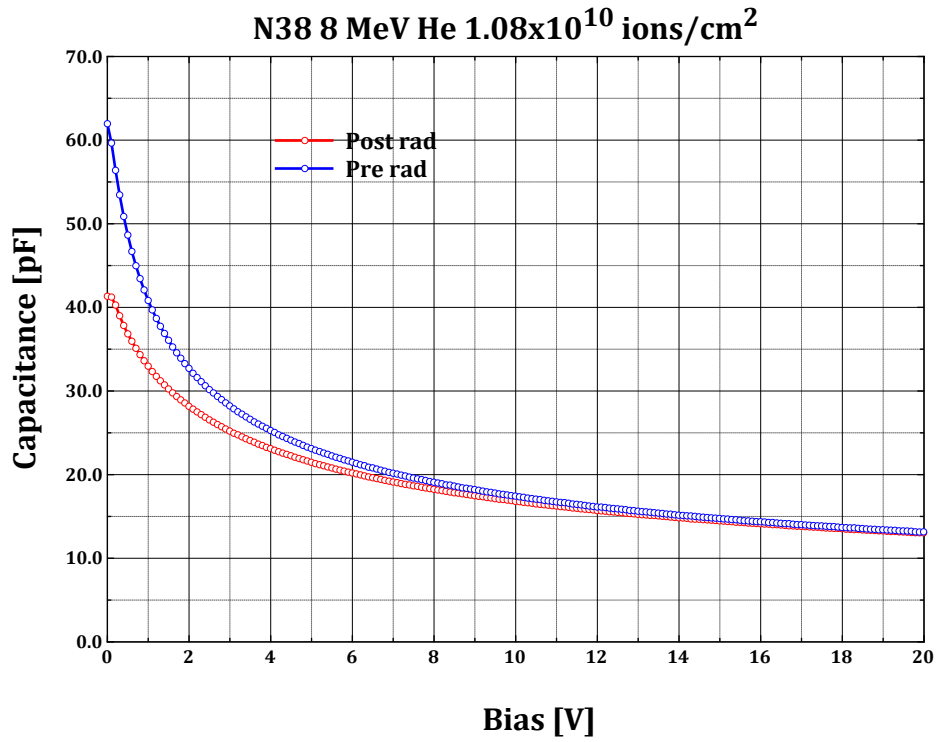

Figure 38 Pre and post irradiation C-V curves 8 MeV He irradiated

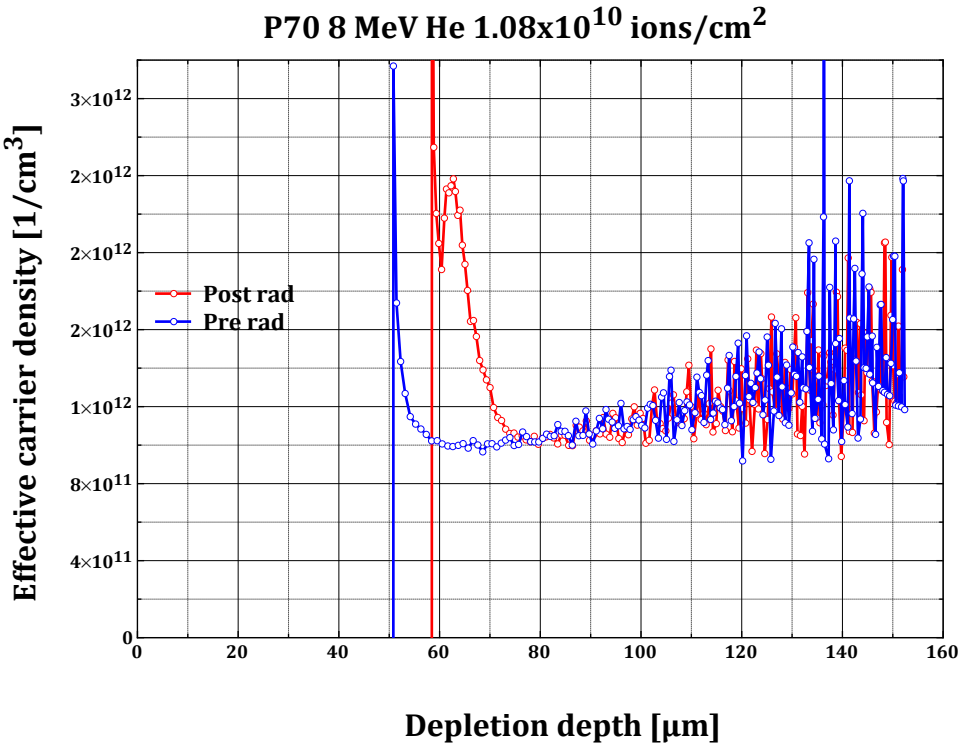

Figure 39 Apparent doping profile dependence on depth for 8 MeV He irradiated p70

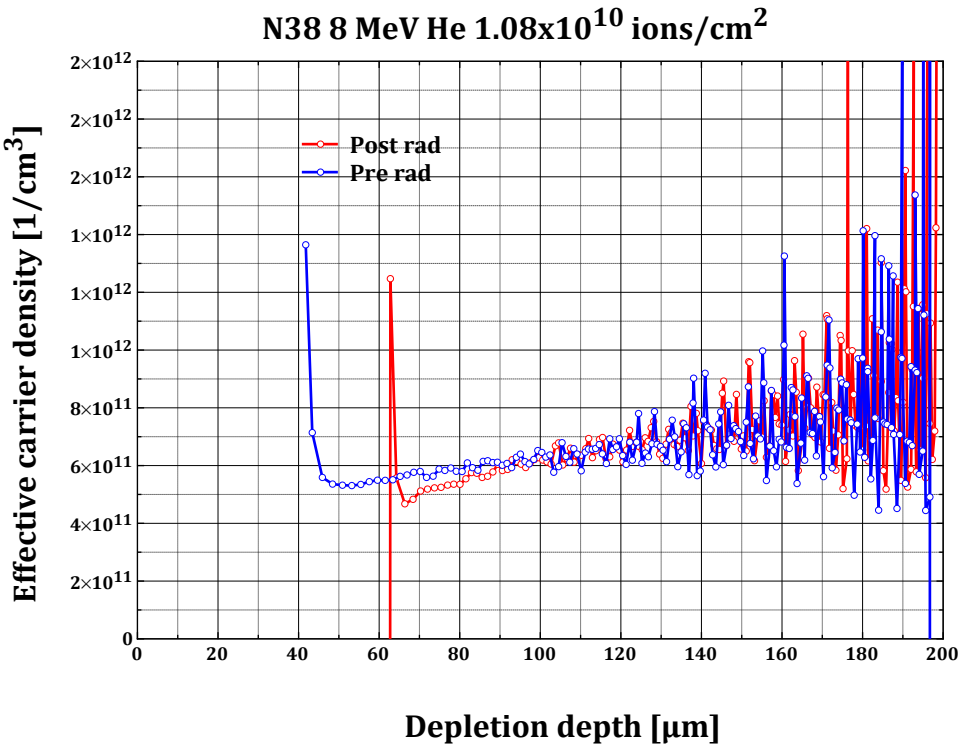

Figure 40 Apparent doping profile dependence on depth for 8 MeV He irradiated n38

The results for the H irradiations are quite different. Since the damage is so high we are not sure if the C-V curves mean anything, so will omit these results here.

We measured bias curves for the irradiated devices where we encountered the same problems as in case of the electron-irradiated devices. Our power supply was limited to 100 V so the actual bias we could put on the devices was very limited, especially for the H irradiated devices. Figure 41 - Figure 43 show the bias curves measured after irradiation. These curves also show higher saturation values than p81 and n26 so we cannot really compare them. In case of the He irradiations the curves are quickly saturating. In case of the H irradiation the leakage current was so large that the 100 V power supply could not even put 1 V actual bias on the devices. Therefore, there is not much value of this data.

This experiment was just a quick effort to see if anything can be observed with full area irradiations. We conclude that it would be worth to repeat these measurements under much more controlled conditions. Unfortunately, we ran out of devices and time.

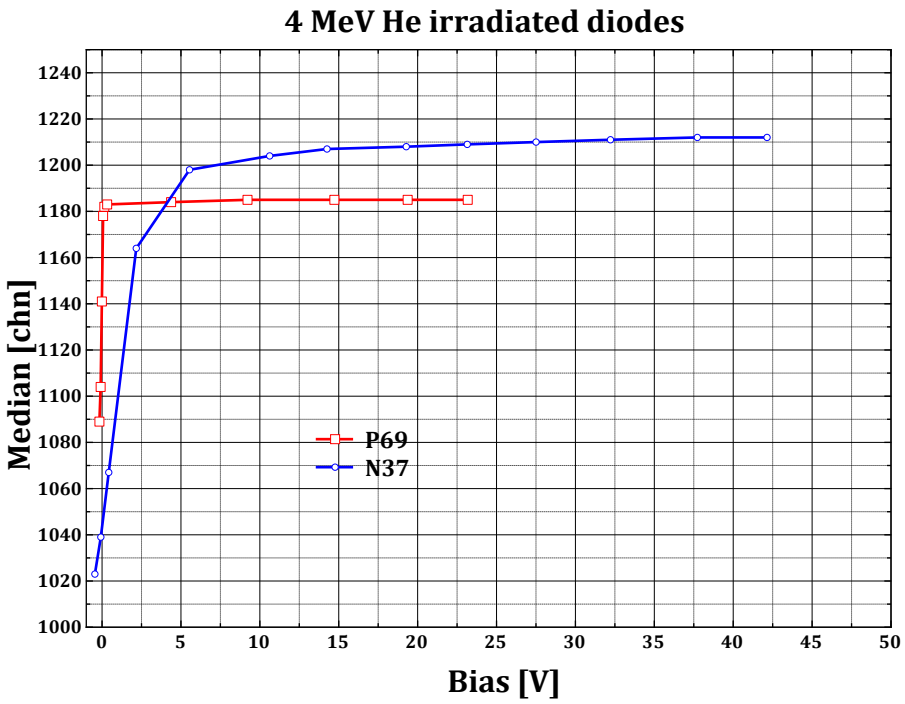

Figure 41 Bias curves for 4 MeV He irradiated p69 and n37

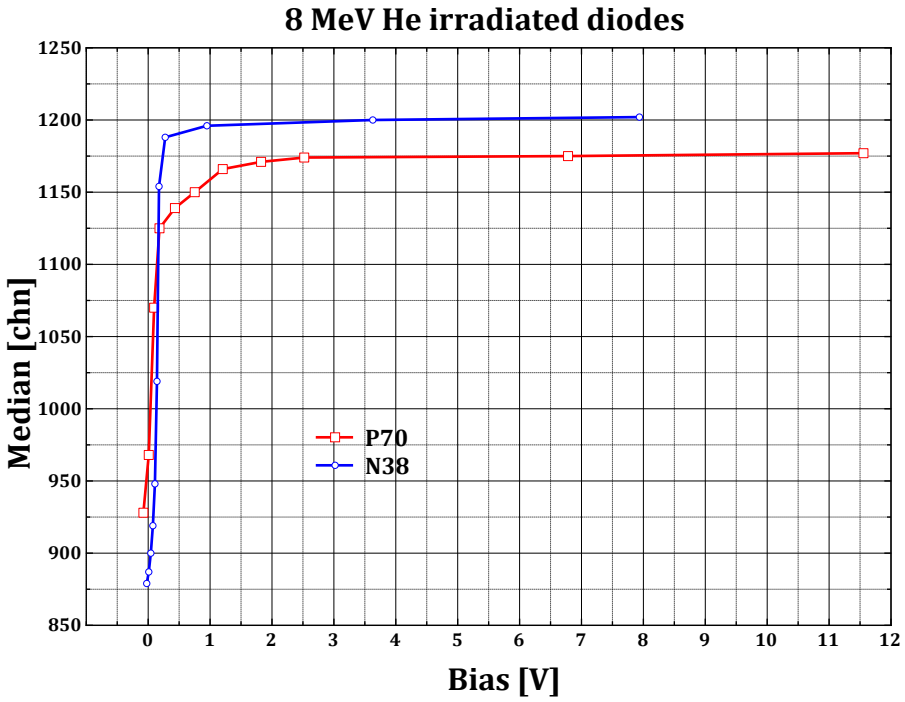

Figure 42 Bias curves for 8 MeV He irradiated p70 and n38

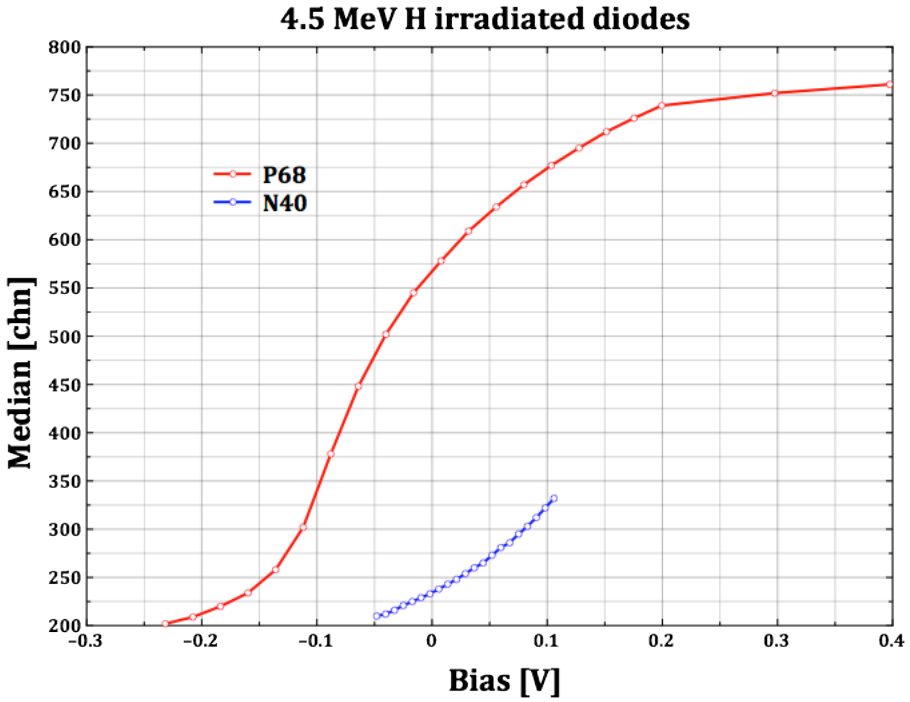

Figure 43 Bias curves for 4.5 MeV H irradiated p68 and n40

Calculation of ionization and damage profiles

We performed SRIM and Marlowe calculations to determine the ionization and damage profiles for the irradiation conditions and the 2 MeV He IBIC measurements. Figure 44 - Figure 47show the ionization and damage profiles. There is a very good agreement between the SRIM and Marlowe ionization profiles, which is expected, since they use very similar stopping power models. Comparing the damage profiles is more complicated since the two programs have different damage models. SRIM uses the displacement energy concept. Atoms that receive larger energy than the displacement energy leave the lattice site with energy of $E = T - E_b$ (where T is the transferred energy and E_b is the bulk binding energy) and leave a vacancy behind. Marlowe uses only the bulk binding energy and at the end of the cascade pairs the interstitial atoms and vacancies and tries to classify them into permanent (distant pairs) and immediately recombining (close and near) pairs. Neither approach is correct for the following reasons:

- SRIM overestimates the number of vacancies because it does not check whether the interstitial stopped in the vicinity of a vacancy (uncorrelated close and near pairs in Marlowe terminology). These pairs will immediately recombine, but SRIM counts them as permanent vacancies.
- Although Marlowe tries to take into consideration the immediate recombination, the recombination radius might be larger than what Marlowe uses (immediate or next to immediate empty lattice site to the interstitial atom). This will result in overestimating the number of vacancies, too.

In order to make a comparison that makes sense we performed the Marlowe calculations setting the EBSD parameter to the displacement energy (pretending that the displacement energy is the bulk binding energy). In this case the total number of vacancies and the profile should be comparable to the SRIM calculations. There are two factors that makes the comparison less than perfect, both due to the fact that Marlowe subtract the displacement energy from the transferred energy:

- The positions of the interstitials will be all wrong; therefore, classifying the pairs into close, near, and distant pairs does not make sense. We have to consider all pairs. It will give a comparable total number of vacancies and vacancy profile.
- Probably there are a few atoms that after subtracting the displacement energy do not have enough energy to create another vacancy. These atoms could have enough energy if only the bulk binding energy had been subtracted. We assume that there very few of them.

The damage profiles from Marlowe and SRIM are quite close, although in all cases SRIM seems to result in more damage than Marlowe. We need to keep in mind that these profiles, both SRIM and MARLOWE, overestimate the actual damage. A more detailed study of the problem will be published in the near future.

From the figures it is clear that in the self-IBIC case only one of the carriers are really affected by the damage (electrons for the p-type and holes for the n-type diodes)[3]. In every case except the 4.5 MeV H beam both the damage and the ionization are contained within the built-in depletion layer (although the 8 MeV irradiation is right at the edge of the depletion delayer); therefore, the carriers drift through the damaged region. In case of the 4.5 MeV irradiation both bulk of the ionization and the damage peak are located in the field free region of the diode at 0 V bias; therefore, one of the carriers needs to diffuse through the damaged region. Hopefully, these different scenarios combined with the in-situ IBIC measurements will help to confirm or improve the Vittone model.

[3] This is not entirely true for the 4.5 MeV H case when there is significant overlap between the ionization and damaged profiles, so both carriers are affected although one is quite a bit more that the other.

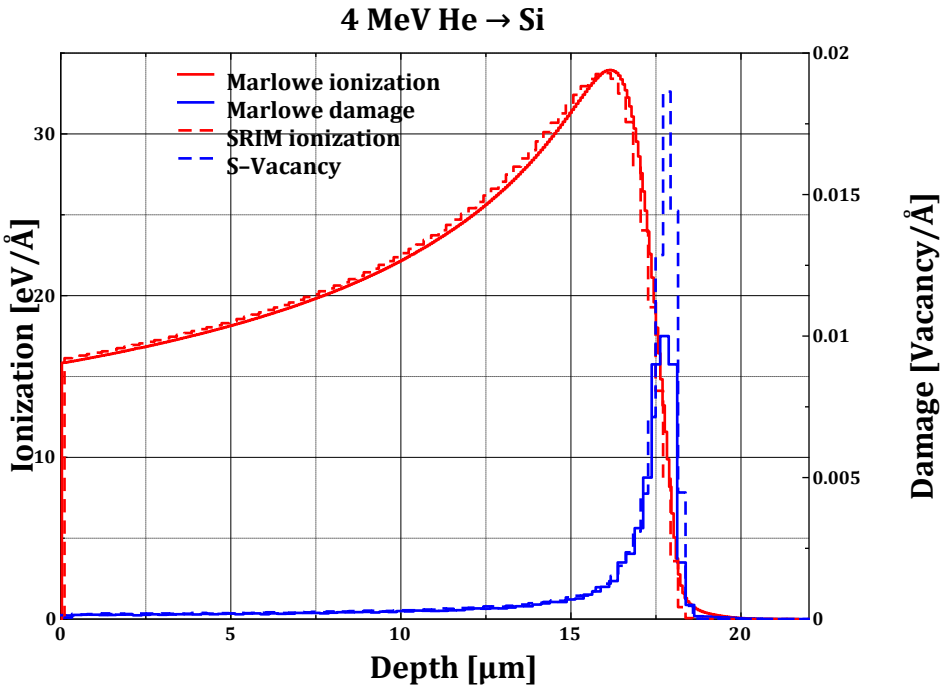

Figure 44 4 MeV He ionization and damage profiles in Si

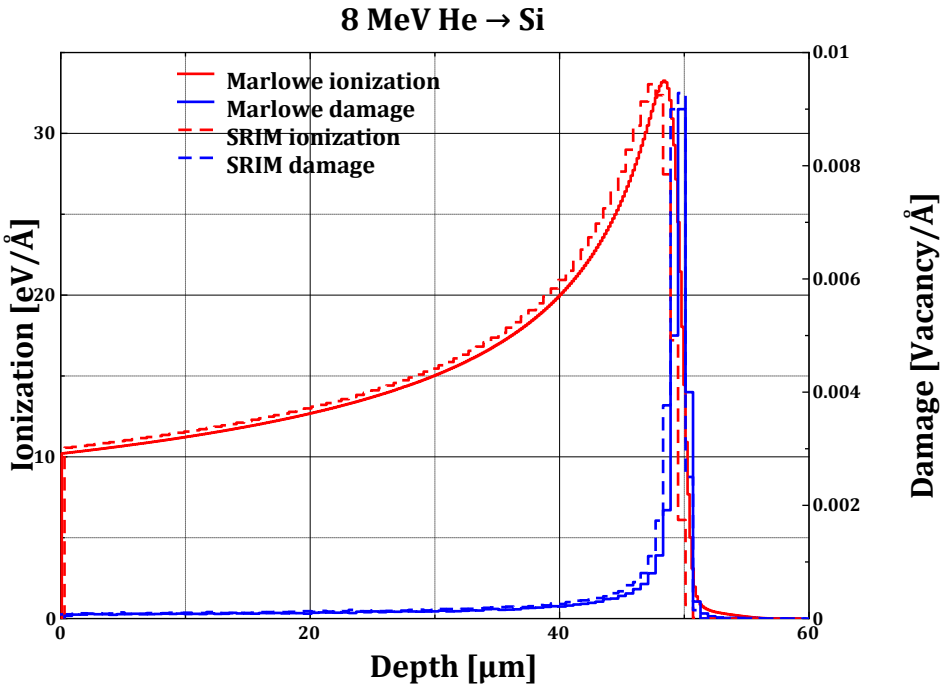

Figure 45 8 MeV He ionization and damage profiles in Si

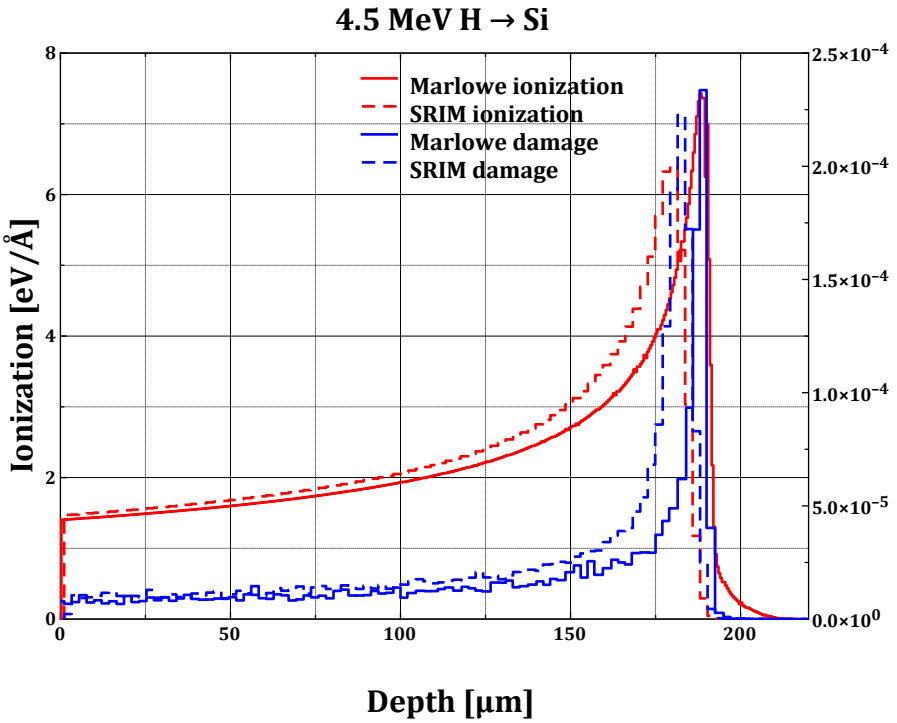

Figure 46 4.5 MeV H ionization and damage profiles in Si

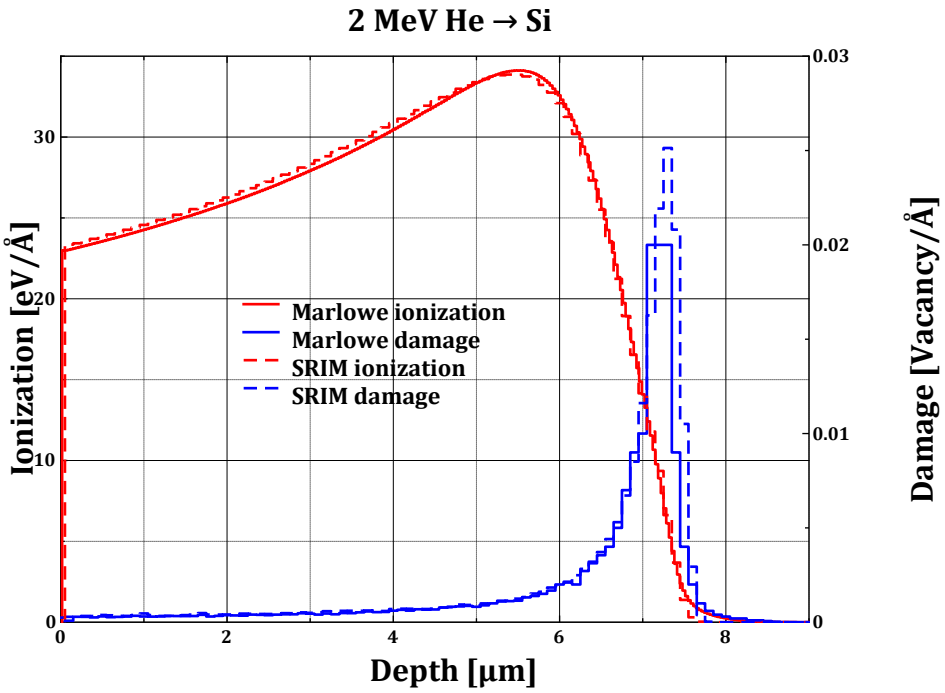

Figure 47 2 MeV He ionization and damage profiles in Si

Figure 48 shows the 2 MeV He ionization profile and the damage profiles for the rest of the beams. This is intended to show that the IBIC modeling is almost a one-carrier problem. The carriers are generated very close to the surface; one of them drifts

quickly to the top electrode practically without recombination[4]. The other type of carrier has to move through the damaged region, which is located at different parts of the diode. These different parts can have even different properties based on the applied bias, fielded or field free regions, which can affect the CCE in different ways. Again we have to note that these different scenarios will provide different challenges to the model.

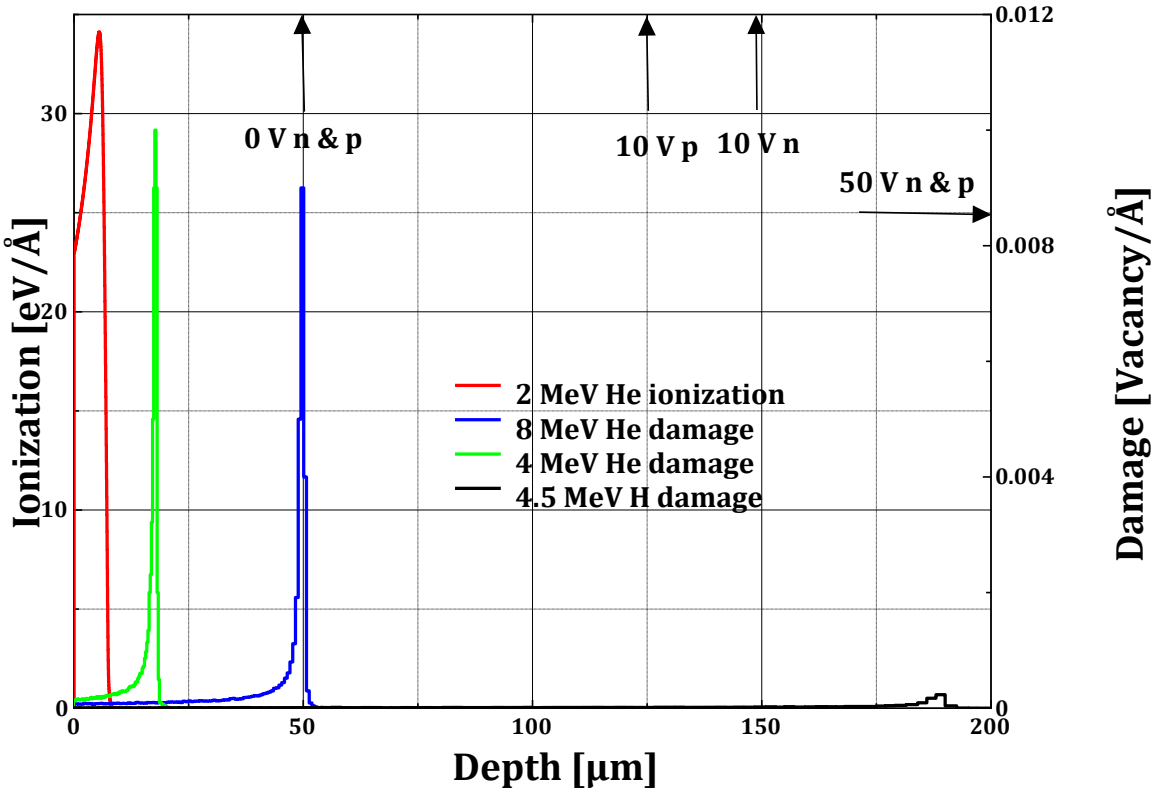

Figure 48 Ionization profile of the 2 MeV He beam and damage profiles of the irradiation beams

We also calculated the ratio of di-vacancies to the total numbers of vacancies. We calculated the clustering for these cases. The definition of a cluster was that every vacancy in the cluster has a neighboring vacancy at the shortest distance in the lattice ($\sqrt{3 \cdot 0.25^2}$ lattice constant). Then we divided the number of vacancies in the cluster by two and rounded down. It is not clear that this is correct (two di-vacancies in a cluster might have different effect on the carries than the effect of one di-vacancy multiplied by two) but it is our best guess.

Figure 49 - Figure 51 show the di-vacancy ratios to the total number of vacancies as the function of depth for the three irradiation cases. The profiles seem to be depth independent apart from the surface region and the very end. The ratios are 7%, 6%, and 2% for 4 and 8 MeV He, and 4.5 MeV H beams, respectively.

[4] Obviously this assumption needs to be tested in the model.

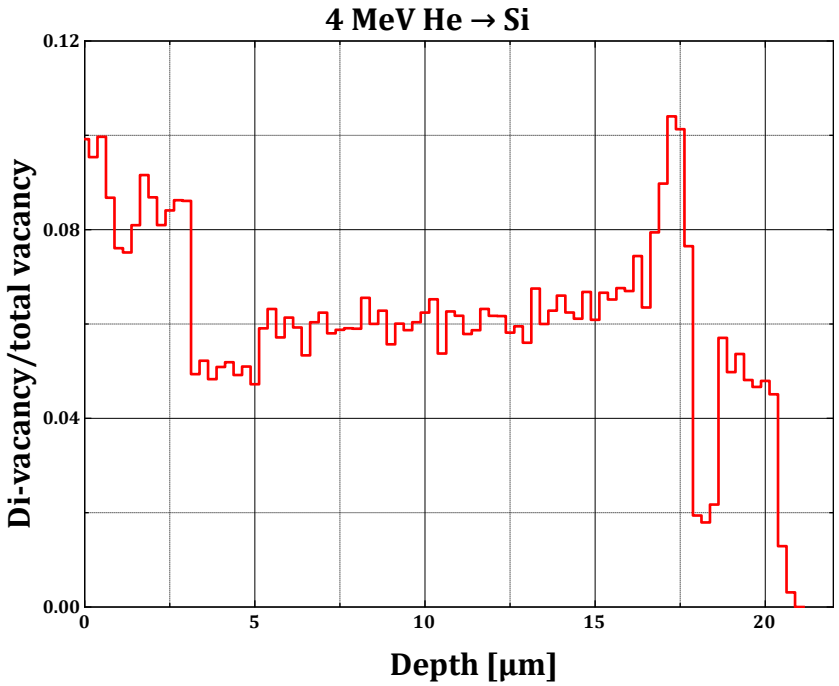

Figure 49 Di-vacancy ratio for 4 MeV He

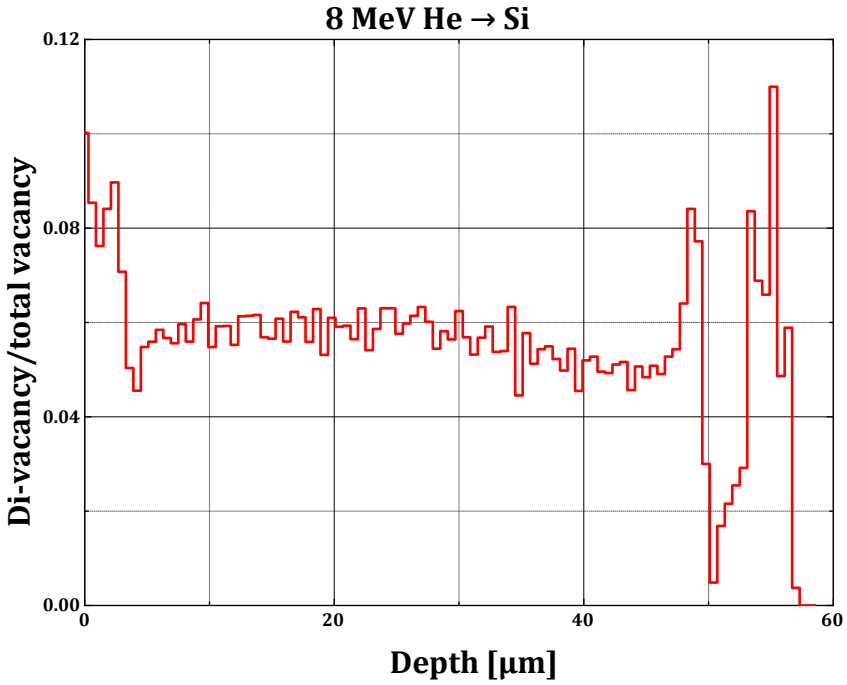

Figure 50 Di-vacancy ratio for 8 MeV He

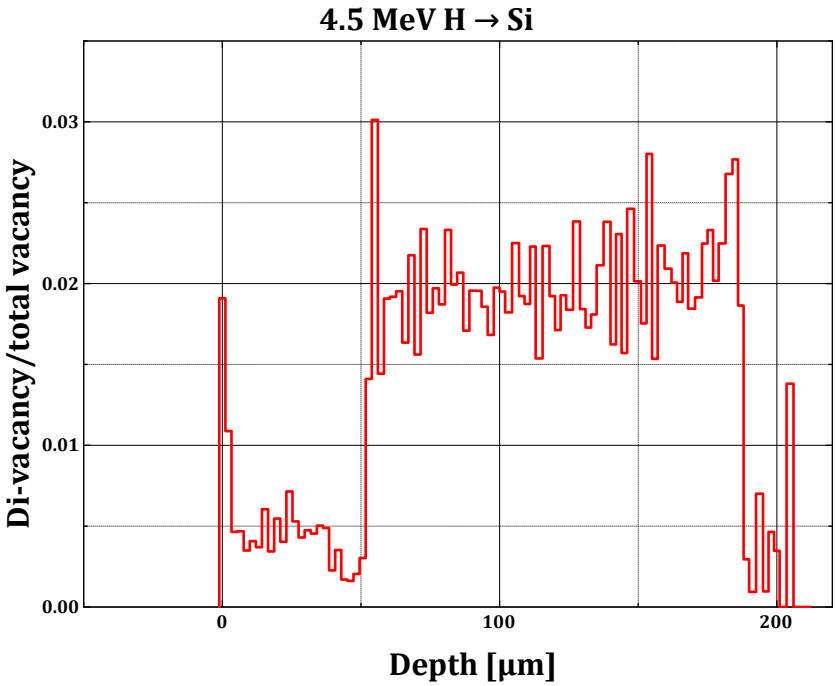

Figure 51 Di-vacancy ratio for 4.5 MeV H

IBIC and C-V characterization of 8 MeV He whole area irradiated Helsinki and Hamamatsu diodes

C-V and DLTS measurements

An n-type Helsinki diode and two Hamamatsu S5821 PIN diodes were irradiated with 8 MeV He ions at ANSTO. The He ion beam was rastered over the devices with ~ 10,000 ions/s, 500 µs dwell time and ~2 µm pixel size. The irradiation patterns are shown in Figure 52.

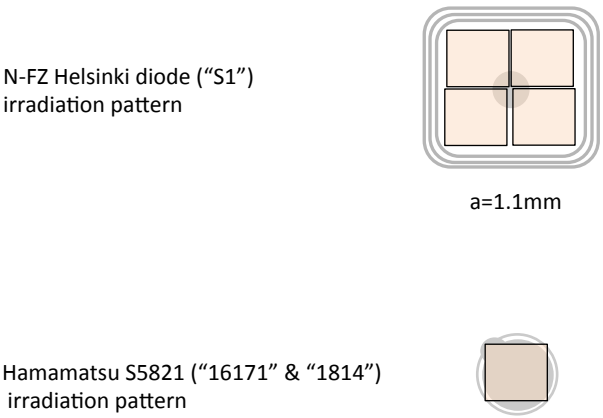

Figure 52 Irradiation patterns for the Helsinki and S5821 PIN diodes

The area of the devices and the irradiation fluence is shown in Table 1, for further details see [5].

Table 1 Irradiation fluences and areas

Device	Area [mm²]	Fluence
N_FZ Helsinki	2.5x2.5	1E+10
S5821 #16171	1.1	1E+10
S5821 #1814	1.1	1E+09

The exact properties of the S5821 diodes are not known apart from the parameters given in the spec sheet available at the Hamamatsu website. Using the parameters and the C-V curve from the spec sheet, we determined that the doping in the intrinsic layer is in order of 10^{13} 1/cm^3 and the depletion layer is around 45 µm at 50 V. At first C-V measurements were performed on all three devices.

Figure 53 shows the C-V curves before and after irradiation. The pre irradiation curve for the Helsinki diode is from another similar diode, and for the S5821 PINs the C-V curve from the spec sheet was used. The change in the capacitance of the Helsinki diode is somewhat larger than the change in a diode irradiated with the 8 MeV He ions at SNL using the pulsed irradiation facility (25 pF ANSTO vs 40 pF SNL) [6]. The reason for the discrepancy can be attributed to the fact that the pulsed

irradiation might not enterily cover the device; therefore, the real fluence was probably somewhat lower than the nominal one.

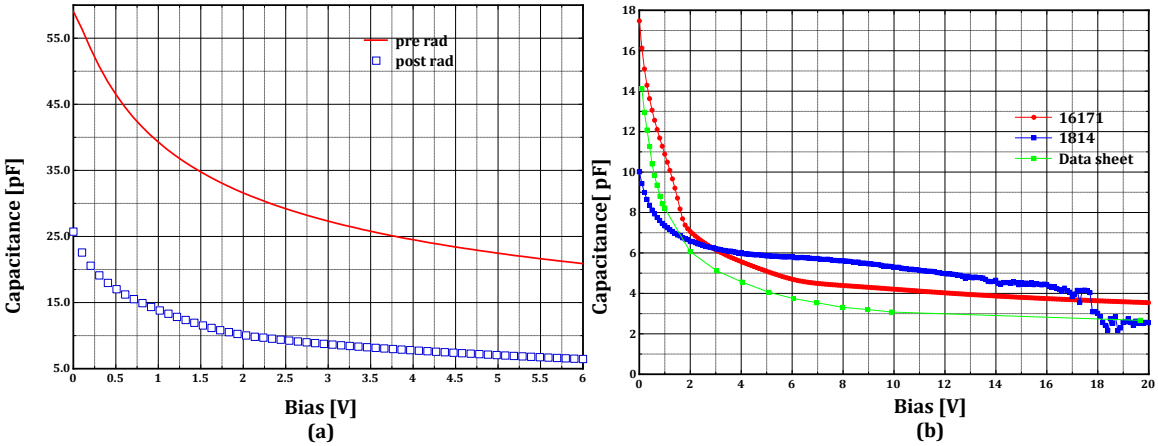

Figure 53 C-V curves before and after irradiation, Helsinki diode (a), S5821 PINs (b)

The C-V curves for the S5821 PINs are more confusing. The un-irradiated C-V curves measured at ANSTO agree quite well with the one from the spec sheet. The usual behavior of the capacitance at 0 V is a decrease in capacitance after the irradiation. For moderate damage usually the capacitance approaches the un-irradiated one at increasing voltages, and for higher damages it was observed that the capacitance after irradiation becomes larger than the un-irradiated one for higher bias values. In this case the behavior of the C-V curves is inconsistent. The lower fluence irradiation (#1814 @ 10^9 ions/cm^2) mimics a high damage case. The higher fluence irradiation (#16171 @ 10^{10} ions/cm^2) does not make much sense; the capacitance increased at 0 V bias. It might be necessary to repeat this experiment.

DLTS measurements were performed on all three devices. The measurement was quite problematic with the Helsinki diode because of its size. The SNL DLTS equipment is designed for devices mounted in TO-18 cans.

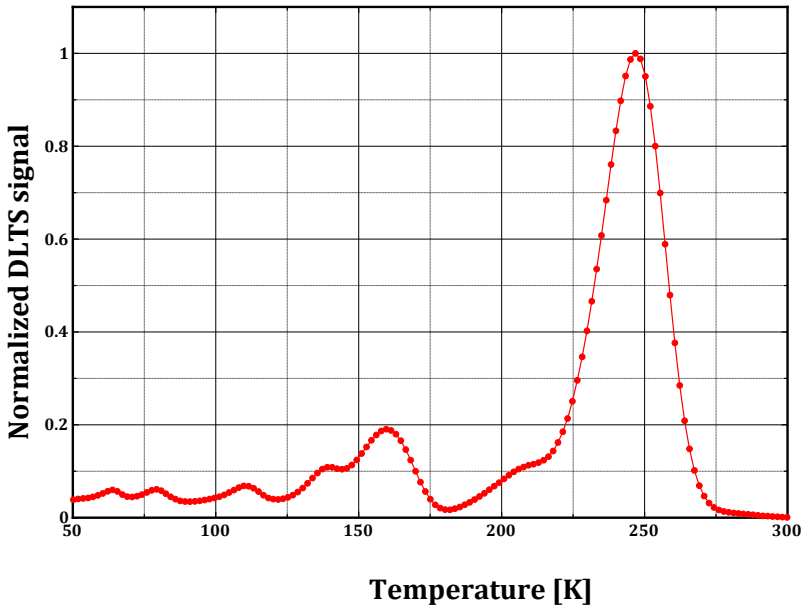

Figure 54 DLTS Spectrum of Helsinki diode after 8 MeV He irradiation

Figure 54 shows a DLTS spectrum of the Helsinki diode. The absolute temperature scale is incorrect, since the device did not have very good heat contact. The spectrum is a usual Si displacement damaged spectrum with the asymmetric V2(--) and V2(-) peaks (see for example [7]). One noticeable feature of the spectrum is the lack of the VO peak at low temperatures, which can be attributed to defect compensation.

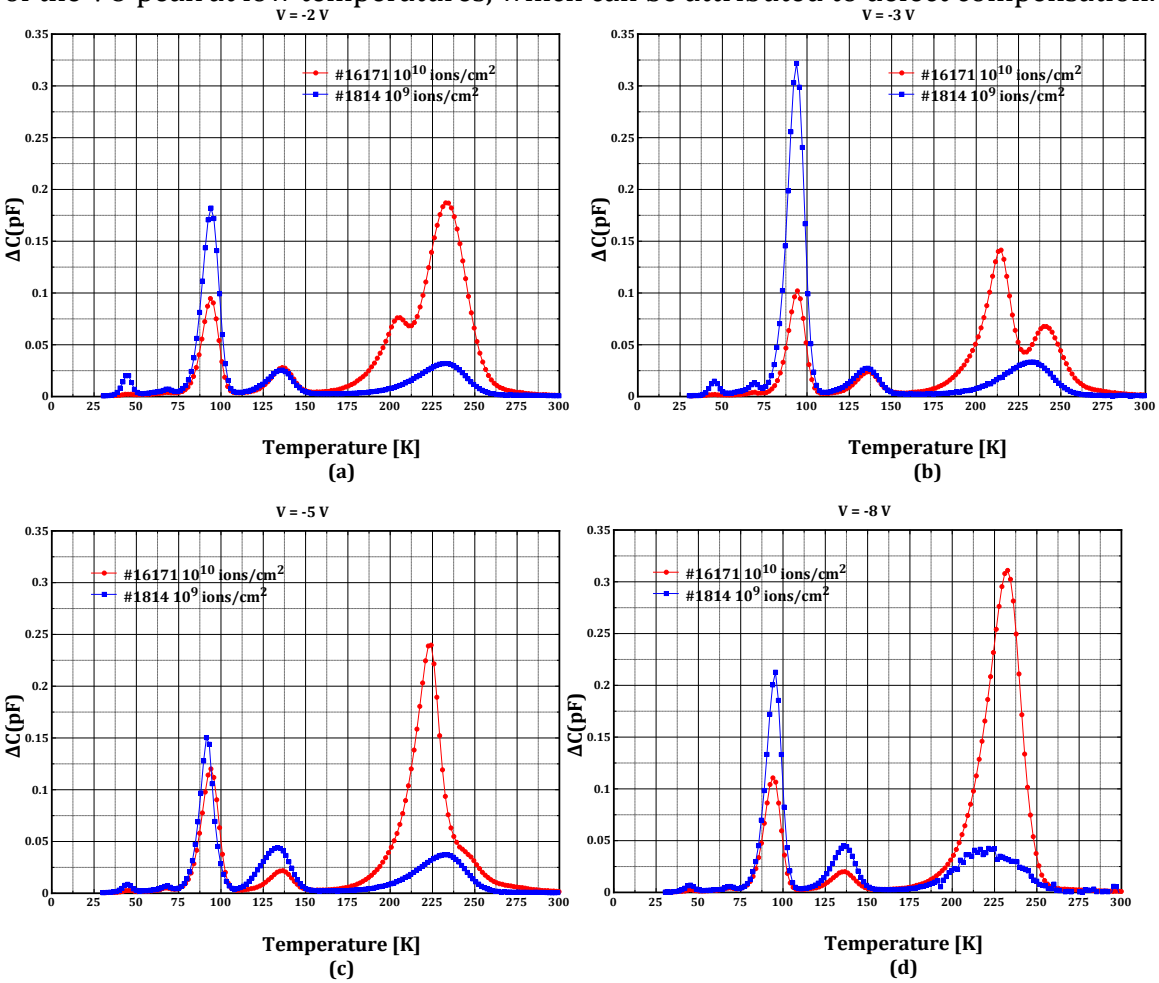

Figure 55 DLTS spectra of S5821 #1814 and #16171 at various bias voltages

Figure 55 shows DLTS spectra of the two S5821 PINs at various bias voltages. By increasing the bias, DLTS probes thicker and thicker layers. With the -2 V to -8 V range the region probed varied from 15 to 20-25 μm. Let's recall that a 8 MeV He ion created the end of range damage (peak in the damage profile) at around 50 μm and it is about 5 μm wide [6]. Therefore it is obvious that DLTS is probing only the region where the damage is uniform and relatively low. What we expect is that the DLTS peaks are growing with increasing bias voltage (more defects are included in the sensitive region). We definitely do not expect a change in the shape of the spectrum. The spectra of #1814 follow quite well this expected behavior. The spectrum shows two V2 peaks with about the same height (indicates no clustering), and they are slowly growing with increasing bias. On the other hand the spectra of #16171 show peaks moving around, which are not the well known DLTS peaks. The C-V curve of #16171 already indicated that there is some problem with this device, and

the DLTS measurement confirmed it. Unfortunately, we do not know much about the structure of the device (such as oxides or passivation layers). One possibility (apart from experimental error) is that there is an oxide layer that has trapped charge in it. This beam generates large amount of electron-hole pairs, of which the holes can be trapped in the oxide and affect both the C-V and DLTS measurements.
At this point it is interesting to have another look at Figure 54. It is quite different from the spectrum of #1814. The DLTS spectrum of #1814 is electron like, while the spectrum of the Helsinki diode is more like the spectrum of a neutron or heavy ion irradiated device. The Helsinki diodes are very low doped (almost two orders of magnitude lower than the S5821) and they are practically depleted to 50 µm at 0V. Applying any voltage will increase the depletion layer further. Since the damage peak is right around 50 µm, the DLTS is actually measuring the end of range damage peak and not the uniform low damage region. The spectrum's shape indicates that at the end of range the damage is more neutron like.
The C-V and DLTS data were sent to RBI and ANSTO for further processing and interpretation.

IBIC measurements

The Helsinki diode got damaged during DLTS measurement; therefore, no IBIC measurement was performed on it. We performed IBIC measurements at 2, 5, and 10 MeV energies. We compared the induced charge to the charge induced in a Hamamatsu S1223 PIN diode, which we routinely use for calibration.

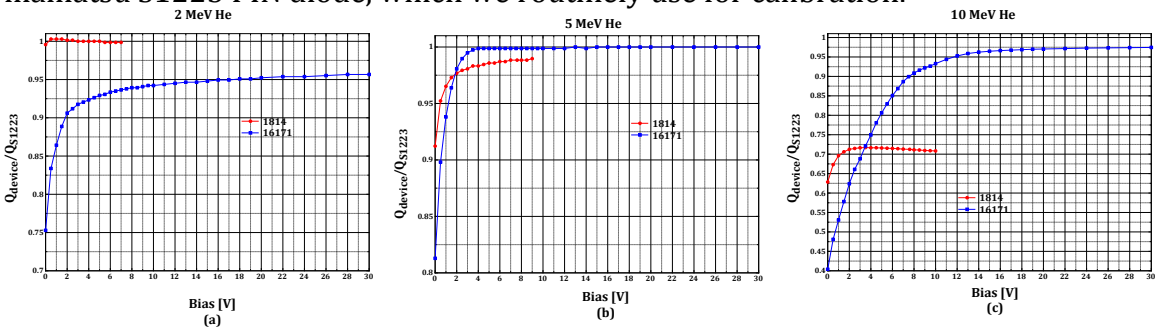

Figure 56 CCE bias curves for 2 MeV (a), 5 MeV (b), and 10 MeV (c) He ions

Figure 56 shows the CCE bias curves for the three energies. Unfortunately, due to the high leakage current of #1814 (although it had the lower fluence), the bias could not be increased over 10 V on this device. The qualitative interpretation of the bias curves for #1814 is relative simple. In the 2 MeV case all the charge is deposited in the depletion layer (which is already around 8 µm even at 0 V) and the induced charge is entirely due to drift. The damage is low enough not to have recombination; therefore, the CCE is very close to 1 and independent of the bias. In the case of 5 MeV the charge is deposited up to 20 µm. When the depletion region is larger than this distance, we have the same case as before, with full charge collection for moderate damage. Unfortunately, device #1814 could not be biased to reach this width due to the leakage current and the 100 MΩ protection resistor in the Ortec 142A preamplifier. When the depletion layer width is less, then only part of the charge is collected by drift, a fraction outside of the depletion layer has to diffuse into the de-

pletion layer, and during diffusion more recombination occurs due to the damage. As the depletion region width increases with bias, so does the CCE. In case of 10 MeV most of the charge is created behind the damage peak, so the carriers have to diffuse through the highly damaged region to reach the junction. Many of the carriers will recombine in the highly damaged region on their way to the depletion region. This explains the greatly reduced CCE.

The interpretation of the #16171 bias curves is more problematic. In principle, for the 2 MeV case the bias curves should have the same shape, although, lower CCE for #16171 if the damage close to the surface affects the recombination during drift. The different bias dependence suggests that the depletion depth dependence on the bias voltage is not the same for the two devices. Our suspicion is that trapped charge in the oxide causes the actual voltage on the device to be different than the applied one (this is not the same problem as above with the leakage current). More analysis of the data is required.

Finally, Figure 57 summarizes the collected charge for the two devices at the different energies at 0 V (built-in depletion layer) and at the saturation voltage. The 1223 PIN collected charge is included for reference. A simple conclusion is that at energies when the charge is generated between the surface and the high damage layer at high voltages the low damage (#1814) does not affect the charge collection. When most of the charge is created behind the high damage region, the charge collection decreases significantly even at high voltage.

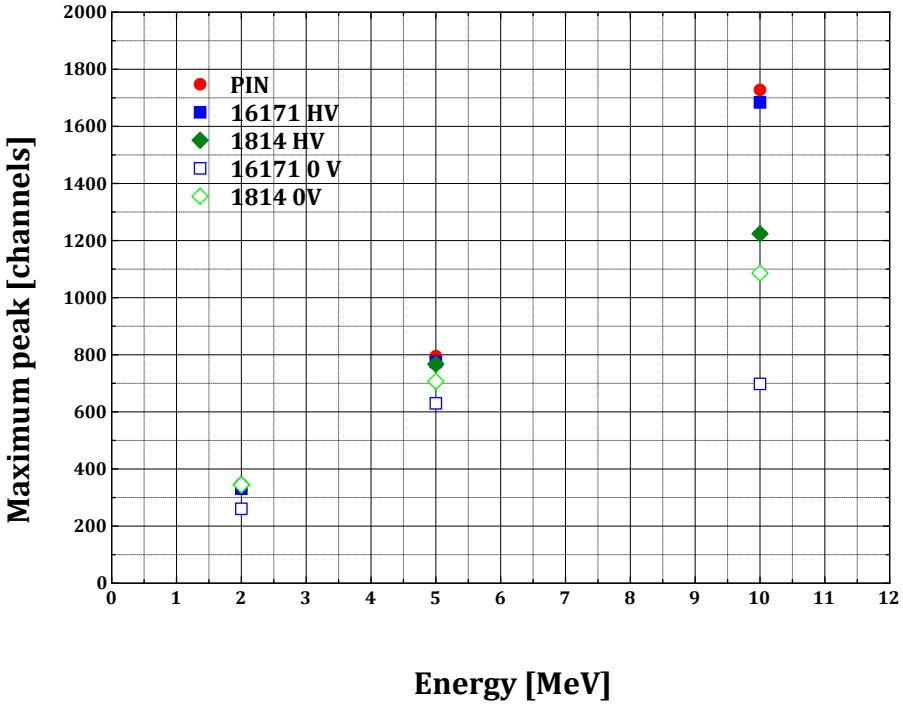

Figure 57 Maximum peaks channels at 0 V and at saturation

Characterization of neutron irradiated Helsinki diodes

Four p-type Helsinki diodes were irradiated with neutrons at the SNL ACCR up to $0.9x10^{14}$ 1 MeV neutron equivalent fluence.

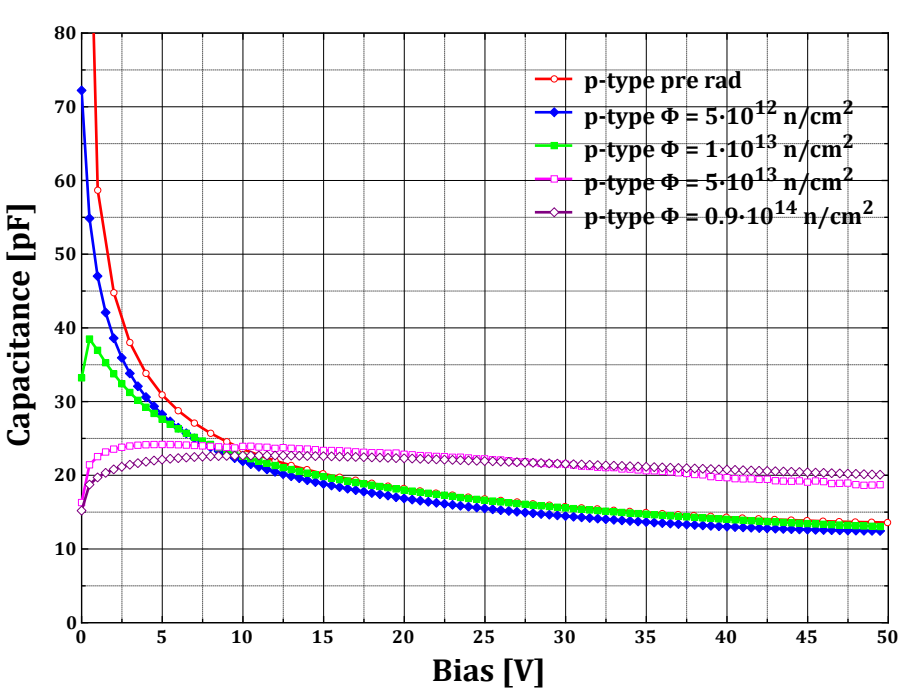

Figure 58 C-V curves of neutron irradiated p-type diodes

Figure 58 shows the C-V curves before and after the neutrons irradiation. It is clear that for the first two fluences the damage is moderate, the C-V curves change as expected, lower capacitance at zero bias and the capacitance gradually approaches the un-irradiated values at higher biases. On the other hand the higher fluences ($\geq 10^{13}$ n/cm^2) seemed to completely destroy the devices, and the C-V curve does not resemble a diode C-V curve anymore. It is somewhat surprising since Si bipolar junction transistors (BJTs) were operable at these fluences [8-10]. The higher sensitivity in this case can be probably attributed to the very low doping of the intrinsic layer.
We attempted to perform IBIC measurements on these diodes using a 2 MeV He beam. All diodes had large leakage current; therefore, we could not put more then a few volts on the device even with an applied bias of 100 V. For the two highest fluences the IBIC signal was in the noise, and nothing could have been measured. For the two lower fluences we could measure a CCE bias curve but we could not determine the actual voltage on the diodes due to the large leakage currents and not precise enough current measurements. Since the un-irradiated diodes are depleted to 50 μm at zero volt, the slowly increasing CCE indicates that the electrostatics of the diode has changed, probably due to charge trapped in the defects.

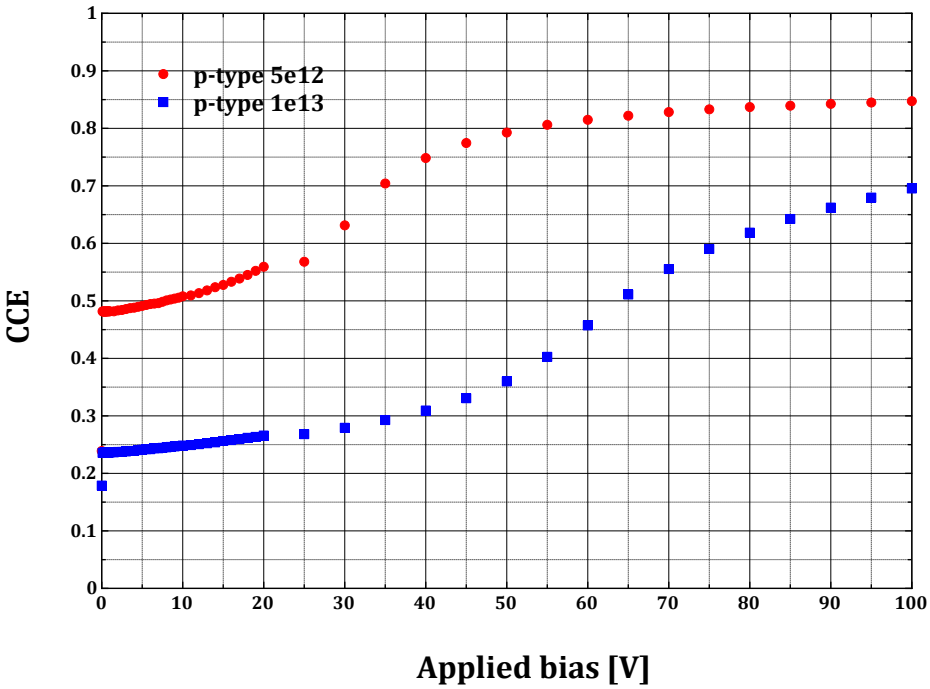

Figure 59 CCE vs. applied bias curves

Search for better devices

As we saw above and will see later, the Helsinki diodes are not ideal. Due the large size the leakage current becomes so large that it is impossible to bias them through the 100 MΩ protection resistor of the Ortec 142A preamplifier. Also, due to the very low doping, even at low damage the defect density can approach the doping density and the charge trapped it the defects can change the electrostatics of the device. Since the C-V and DLTS information is important in addition to the IBIC measurements, to avoid these problems we need to do separate full area irradiations for C-V and DLTS and microbeam irradiations for IBIC (although in this case the electrostatics still changes locally, but it is not clear how much problem this poses for modeling). In addition, due to the large size of these diodes the full area ion irradiation is difficult and time consuming. They have the one major advantage that we know quite a bit about the structure and the manufacturing process [2].

We considered three devices, two Hamamatsu PIN diodes (S5821 and S5973) and a Hamamtsu PN diode (S2368). We selected S5973 and S2386 because we already had them and structural analysis and doping profile determination were performed on them. The S5821 was selected because it was already used in the ANSTO full area irradiations. The devices were irradiated in the SNL ACCR with the same fluences as the p-type Helsinki diodes. This test seems to be the most brutal, since the damage is done in the entire volume of the diodes.

All three diodes are relatively small, with an area in order of 1 mm^2. The doping profile of S5793 and S2386 were measured in the past by spreading resistance measurements, and they are shown in Figure 60 with the bias dependence of the depletion depth.

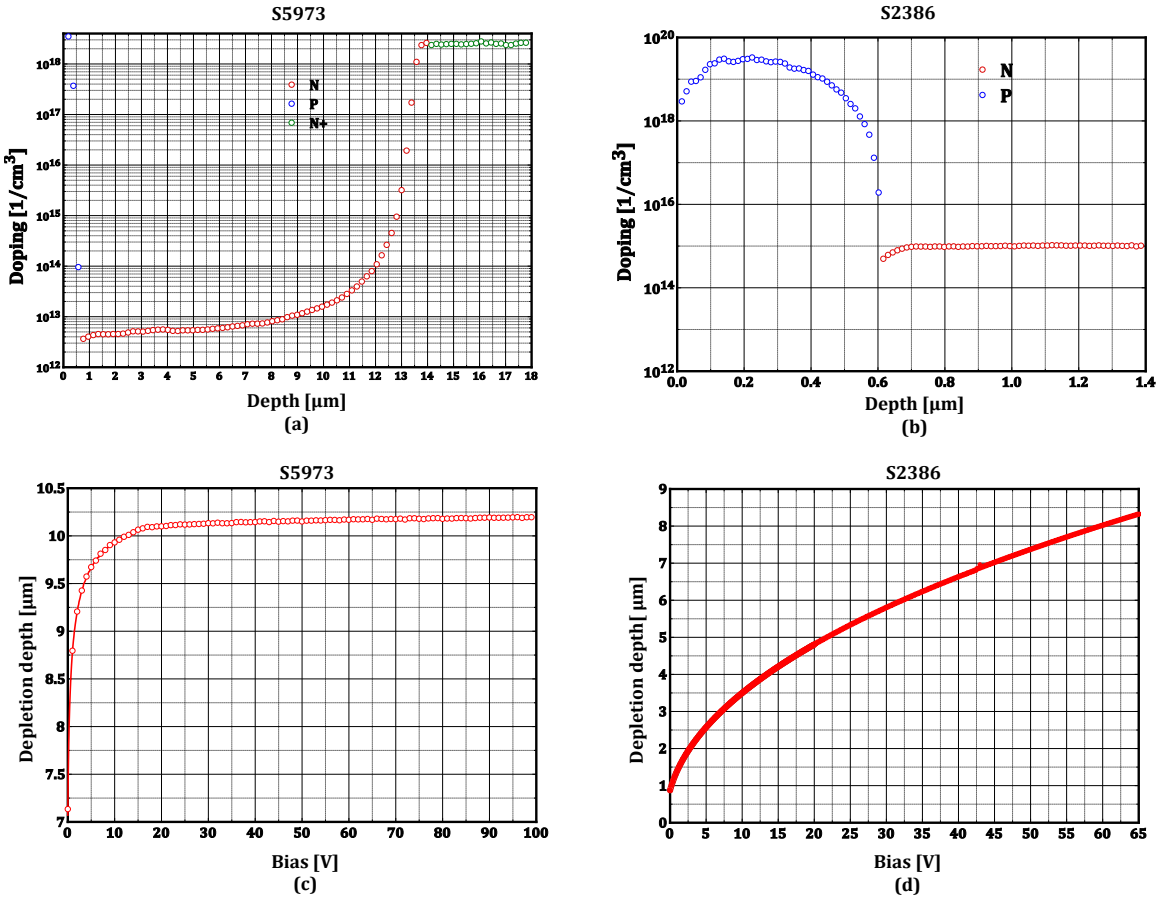

Figure 60 Doping profiles and depletion depth vs. bias for S5973 and s2386

The S5963 is PIN diode with a doping level of 0.5-1x10^{13} 1/cm^3 in an approximately 10 µm thick intrinsic layer. It is fully depleted at ~ 20 V and already 7 µm is depleted at 0 V (which means that at even 0 V all the charge from the 2 MeV He is created in the depletion layer. The S2386 is a P+N diode, which is depleted to 1 µm at 0 V and about 8.5 µm at 65 V. Above this bias the device started to break down. So in this device we were expecting to see a strong bias dependence of the CCE for 2 MeV He ions.

For the S5821 PIN we do not have a doping profile analysis, but the C-V curves indicate an intrinsic layer with a doping of ~10^{13} 1/cm^3. It also shows that the device is depleted to ~6 µm at 0 V and about 45 µm at 50 V.

We performed IBIC measurements with a 2 MeV He beam before the neutron irradiation as the function of bias voltage shown in Figure 61. The results are more or less what was expected; for the PIN diodes there is practically no bias dependence, the depletion layer at 0 V is already thicker than the region where the He ion deposits the charge.

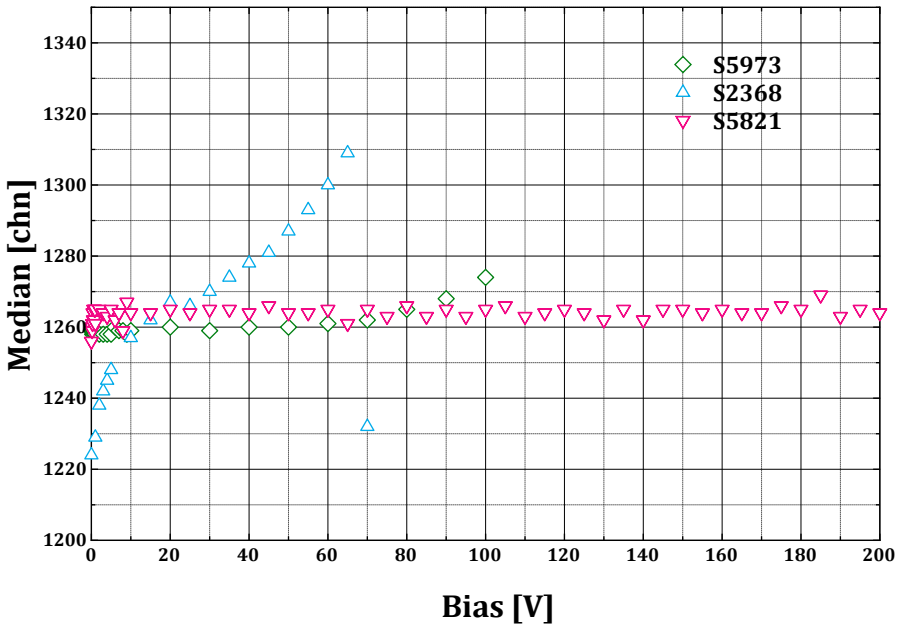

Figure 61 CCE bias curves for S5973, S5821, and S2386 before neutron irradiation

The S2386 also shows the expected bias dependence but after saturating it starts growing again and the IBIC signals becomes larger than the maximum available charge. This behavior indicates avalanches due to impact ionization.

The devices were irradiated with neutrons up to a 1 MeV neutron equivalent fluence of 0.9×10^{14}. During the irradiations three of the S5973 diodes became damaged. C-V measurements were performed on the remaining parts. The C-V curves for S2386 practically did not change at all; the C-V curves for the other devices are shown in Figure 62.

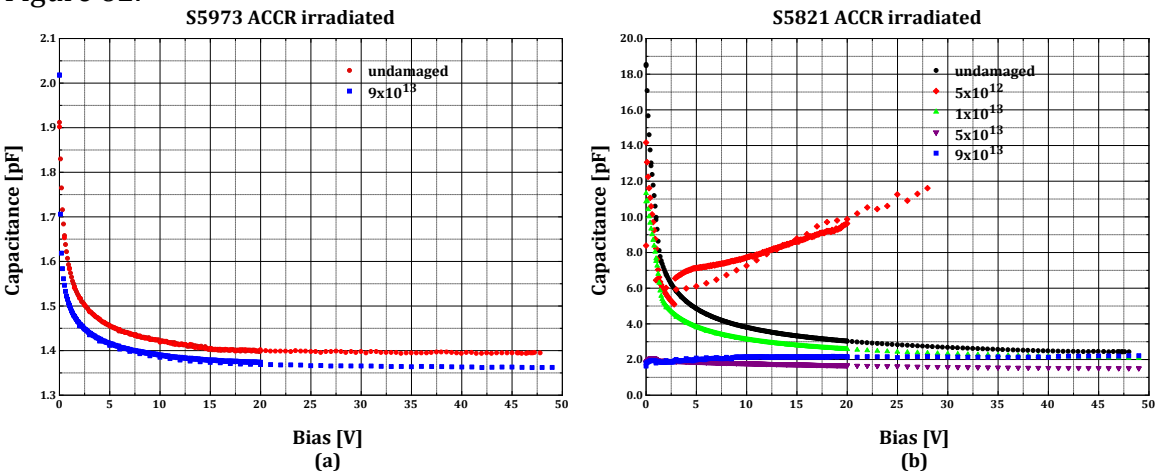

Figure 62 C-V curves for neutron irradiated S5973 and S5821 PINs

The C-V curve for the S5973 irradiated with the highest fluence showed very little change, but when it was placed in the vacuum chamber it became a short circuit. The C-V curves of S5821 indicates that something is wrong with the device irradiated with the lowest fluence, and the two highest fluences show that the devices are

practically dead. We performed IBIC on the three remaining S5821 PINs and all the four S2386 PNs, the bias curves are shown in Figure 63.

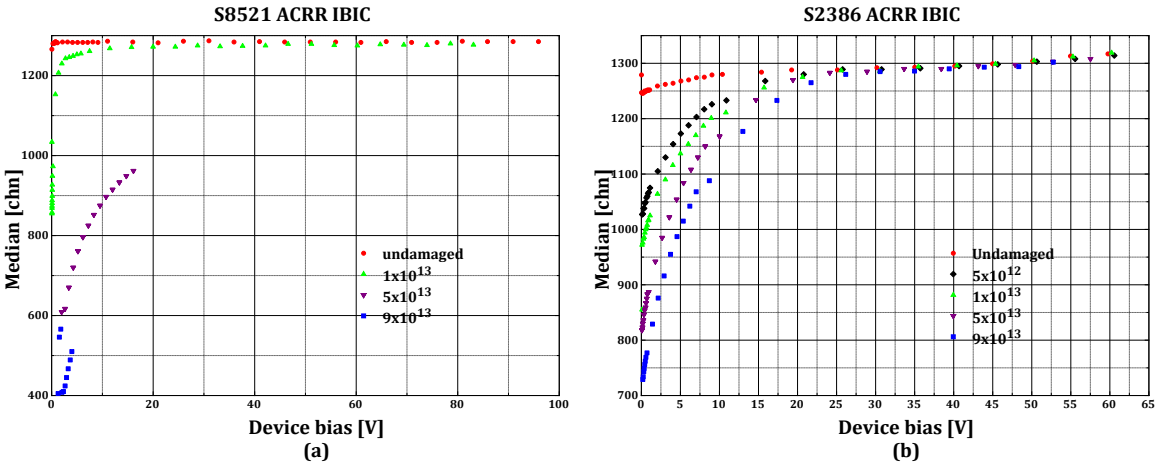

Figure 63 IBIC bias curves for neutron irradiated S8521 (a) and S2386 (b) devices

Although the high fluence S5821 devices seemed to be dead from the C-V curves, we could measure 70 % and 38 % charge collection efficiency at the highest bias we were able to put on. These devices had very large leakage current, several hundreds of nAs at less than 20 V. Also the shapes of the curves indicate that the damage (trapped charge) significantly changed the electrostatics of the device. The S2386 bias curves look exactly as expected. It is worth noting that the increase above the maximum deposited charge is still present, although it is harder to see due to the different scale. Based on the above we think that the S2386 would be a much better device for this project than any of the others, including the Helsinki diodes.

Improvement of damage calculations with Marlowe[5]

Most Binary Collision Approximation (BCA) codes use the concept of displacement energy, which is the energy that an atom has to overcome to be replaced permanently. Originally Marlowe used the same concept [1]. Unfortunately, most people read only this paper and use Marlowe based on it. In the 80s the code was changed and the displacement energy concept was removed and a pair classification scheme was introduced. The authors realized that the displacement energy is not a very good concept, at least not in this environment, and there is a better way to handle it. For example, in Si the displacement energy is dependent on the direction of the recoil, and it can be anything between 12 to 32 eV. Let me quote here Marc Hou (one of the contributors and frequent user of Marlowe) [11]:

"In the case of Frenkel pairs production, an energy threshold was found experimentally below which no Frenkel pair is produced. This suggests an energy threshold value for BCA computations. Unfortunately, this threshold value was found to be dependent on the direction in which momentum is given, which was also predicted by

[5] This work was mainly done for another project, but it has important implications for this CRP; therefore, we include here a brief description.

MD. Thus, depending on direction, the mechanisms involved in producing Frenkel pairs is different, and, therefore, its quantitative estimate for BCA calculations is ambiguous."

When an atom is displaced from its lattice site and stops in a non-lattice position it distorts the lattice. If there is a vacancy nearby, recombination puts the lattice in an energetically more preferable state, like the lattice "pushes" the interstitial into the vacancy [12]. The question is what is nearby? This nearby is what we can call the recombination radius discussed in several papers [13-17]. Marlowe's approach is to pair each interstitial with a vacancy and classify them as close, near, and distant pairs [18]. It assumes that anything other than the distant pairs will recombine in a very short (ps) time scale. This does not really define a recombination radius. Marlowe has three binding energies, specified in the EBND parameter.

- EBND(1) – this is the normal binding energy
- EBND(2) – this is the binding energy for an interstitial or impurity atom. It is not really important since the probability of a recoil colliding with another, stopped recoil is very, very low.
- EBND(3) – this is the binding energy in a replacement collision.

The argument using a different binding energy is that in a replacement collision the state of the lattice does not change; therefore, no energy needed to be removed from the energy of the moving atom. Initially 0 eV was used, but they found that it overestimates the displacements (compared to MD). Now it is said that it is a small amount, less than EBND(1). According to Robinson [19] EBND(1), the normal binding energy is the cohesion energy, which is 4.63 eV for Si

The first task was to determine what EBND(3) is. We calculated the total number of displacements with Molecular Dynamics (MD) and Marlowe, Si into Si at energies from 500 eV to 10 keV. In the Marlowe calculations we varied the EBND(3) parameters from zero to EBND(1). Then we picked the EBND(3) value that gave the closest number of total displacements to the MD calculations. The calculations gave 1.68 eV as the best EBND(3) value with a standard deviation of 0.13 eV.

The next step was to calculate the permanent Frenkel-pairs with MD. A Frenkel-pair was considered permanent if it was present at the end of the calculation (100 ps after the recoil was started). Marlowe calculations were performed and the separation distribution was created for all the pairs. Figure 64 shows the integrated separation distribution for the 5 energies we used in the calculations. What seemed surprising at first sight is that all five distributions are very similar, practically the same. Thinking about the recoil creation process a bit more gives the obvious explanation, which is that most of the vacancies are created by the low energy recoils whose distribution is independent of the initial particle energy (at least in this energy range). We compared the number of permanent Frenkel-pairs from the MD calculation to these distributions and determined a cut-off distance. This distance turned out to be 7.4±0.09 Å, 1.36 times the Si lattice constant.

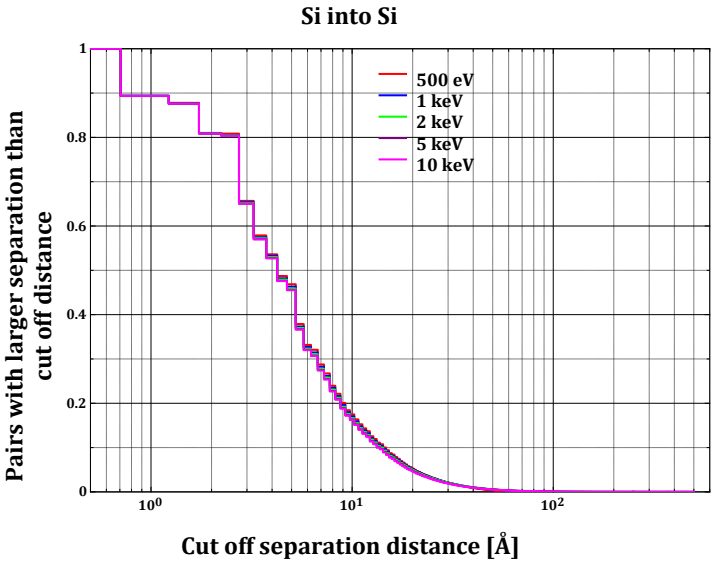

Energy	Cut-off distance
500	7.44
1000	7.42
2000	7.25
5000	7.41
10000	7.47
Average	7.398
Stdev	0.086
Percentage	1.16%

Figure 64 Separation distance distribution

It is interesting to see how the number of permanent Frenkel-pairs distributed between the different Marlowe pair classes. Table 2 shows what fraction of the different classes of Marlowe pairs survived the cut-off process. Not surprisingly the near and close pairs were all eliminated by that process. However, almost all correlated distant pairs were also eliminated (> 95 %). On the average, only ~50 % of the distant pairs become permanent Frenkel-pairs, so Marlowe overestimates the damage by a factor of two if one considers all the distant pairs. More details can be found in [20].

Table 2 Survival rate of different classes of Marlowe pairs[6]

	500 eV						
	Correlated close	Uncorrelated close	Correlated near	Uncorrelated near	Correlated distant	Uncorrelated distant	Total
Recombined	3.97	1.31	3.97	6.19	4.17	6.22	25.83
Survived	0.00	0.00	0.00	0.00	0.22	9.88	10.10
Survival ratio	0.00%	0.00%	0.00%	0.00%	4.99%	61.39%	28.11%
	10 keV						
	Correlated close	Uncorrelated close	Correlated near	Uncorrelated near	Correlated distant	Uncorrelated distant	Total
Recombined	65.84	25.19	65.84	115.90	64.96	109.64	447.38
Survived	0.00	0.00	0.00	0.00	2.96	157.38	160.35
Survival ratio	0.00%	0.00%	0.00%	0.00%	4.36%	58.94%	26.38%

[6] Correlated pairs have the interstitial originated from the paired vacancy, uncorrelated do not.

TCAD (ATLAS) modeling of the Helsinki diodes

In order to check the CRP's 1D model of IBIC in damaged Si diodes we used ATLAS [21] to model the diode in 2D. We created a full-length diode but only 20 μm wide to minimize the number of nodes needed. The initial IBIC calculations showed a huge plasma effect, the e-h plasma pushed out the electric field outside of the plasma and the IBIC current lasted up to a few μs. The electric field was restored when the plasma density became comparable to the doping density. This was very troubling because the electric field changed drastically and the CRP model assumes that the e-h plasma does not disturb the field. Since the decrease in the e-h plasma density was due to its diffusion, the size of the simulated device can have a large effect.

Electrostatic model of the device

After consulting with S. Rath (University of New Delphi was also working on an ATLAS simulation, although not IBIC) we decided to adopt their model [22]. They were modeling half of the entire device with all the guard rings. We decided to model the entire device width to investigate the plasma effect. Unfortunately, ATLAS did not let us do that; it has a node limit and the guard ring implantations used up too many nodes. Since none of the experiments were using the guard ring we eliminated them. We studied the effect of the guard ring and the size of the device on the electrical parameters of the diode and found that there is very little effect. The doping profiles were taken from [23] with changing the doping density in the intrinsic layer to 3.07×10^{11} 1/cm^3. This value gave the best agreement with the measured C-V data. In the University of New Delhi simulation the leakage current was orders of magnitude lower than the measured one. We found that was due to the very long carrier lifetime they used. We varied the carrier lifetime and found that 380 μs gives a very good agreement with the experimental data. We have to note that this value is an order of magnitude smaller than the one given in [2].

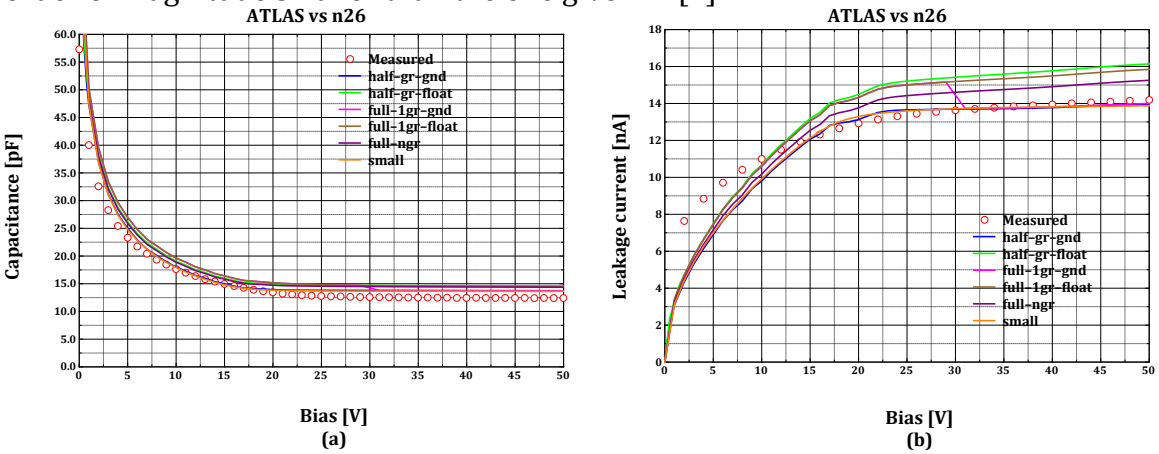

Figure 65 Experiment and ATLAS simulated C-V (a) and I-V (curves) for the various configurations

Figure 65 shows the ATLAS calculated C-V and I-V curves in the different configurations[7] compared to the measured data on diode #28 (n-type). The model shows excellent agreement with the experimental data and practically there is no difference between the different configurations. The calculated electric field, potential, and carrier densities are in good agreement with E. Vittone's 1D model [23].

IBIC simulation in 2D

We modeled the IBIC signal due to a 2 MeV He ion strike at 50 V bias. The device is completely depleted at this bias. ATLAS needs an electron-hole generation term as the functions of space and time (it is a C function that the ATLAS C interpreter compiles for the software). We calculated the 2D ionization energy loss profile using SRIM [24] (it has more precise stopping power than Marlowe) and fitted to a Gaussian around the center of the track with the standard deviation as the function of depth. Figure 66 shows the depth dependence of the charge created per unit length and the spread around the center of the track. This is the spatial dependence of the generation term. SRIM cannot provide temporal information, but fortunately Marlowe can. Figure 67 shows the probability distribution of the slow down time for 200,000 He ions. The median of the distribution is ~ 3 ps, which we chose as the duration of the e-h generation.

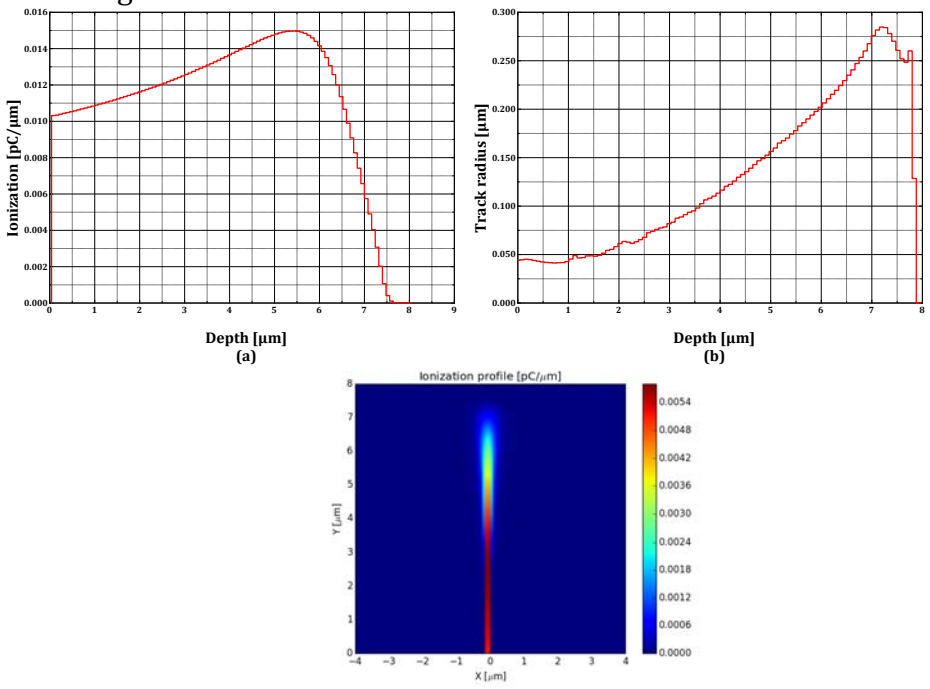

Figure 66 Depth dependence of ionization loss and radial spread

[7] The different configurations were: half diode with 1 guard ring grounded and floating scaled up to the full diode, full diode with 1 guard ring grounded and floating, full diode no guard ring, 20 µm diode scaled up to the full diode.

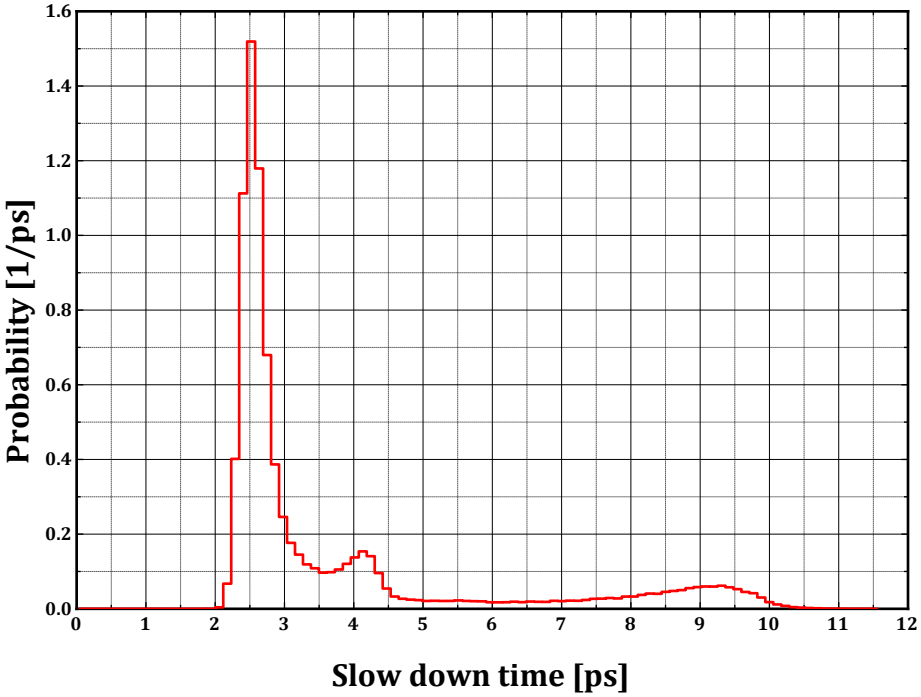

Figure 67 2 MeV He slow down time distribution

Figure 68 shows the simulated IBIC currents for the two configurations. Later we will discuss the validity of the simulation; at this point we just try to understand what we see.

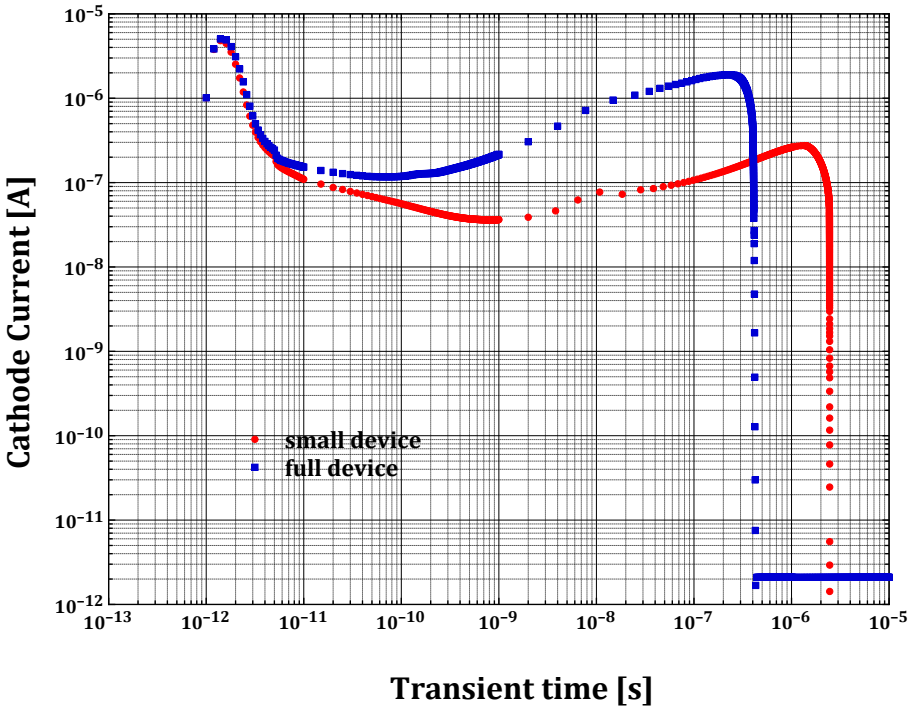

Figure 68 IBIC currents from two different configurations

In both cases there is a sharp pulse at very short times (the He ion hit the device at t = 1 ps), and then there is a long sustained current for relatively long times. For the small device it is a bit over 2 μs, for the full device it is about 300 ns, while for the full device with high doping the current lasts for hundreds of ns. This clearly illustrates the effect of size. We will only concentrate on the real device in the rest of the discussion.

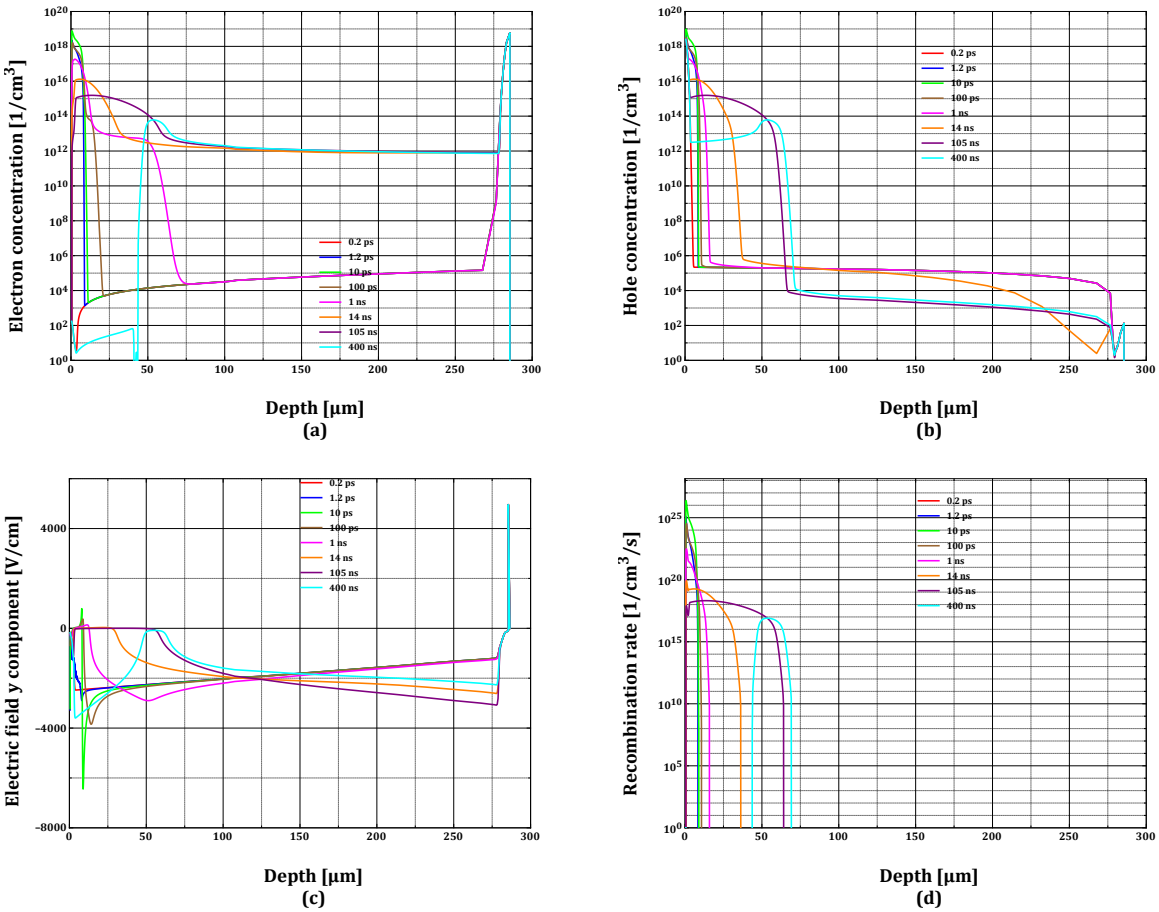

Figure 69 Carrier concentration, electric field, and recombination rate at selected times during the transient

Figure 69 shows the carrier densities, electric field, and recombination as the unction of the distance from the anode along the center of the ion track at various times during the transient. The first two curves (red and blue) are before the ion strike and right after it. By examining these curves (and the 2D distributions that will be presented at the RCM) we can interpret what is happening. The entire intrinsic layer is depleted; therefore, the charge density is the doping level, $3x10^{11}$ $1/cm^3$. When the ion hits in a very short time high-density e-h plasma is created from the surface to about 6 μm deep in the device. The electron and hole densities are several orders of magnitude larger than the doping density. At the edges of this plasma the e-h pairs are quickly separated (it initially happens in the plasma, too, but it does not create net charge) and large net charge will be present at the edges. Due to this much higher charge density than the ionized donor density, this will determine the

electrostatic properties of the devices. The electric field will be concentrated at the edges and it will be zero inside of the e-h plasma. Since the electric field is drastically changed, the Gunn theorem [25] cannot be used to describe the IBIC process. Since there is no field inside the plasma column to separate the electrons and holes, they are diffusing together toward the cathode and laterally. This movement of electrons and holes together is clearly visible in Figure 69 (a) and (b). Since this plasma density is still many orders of magnitude larger than the doping concentration, the plasma pushes the electric field ahead of itself (like a snow plow) toward the cathode as can be seen in Figure 69 c. The e-h separation occurs only at the edges. When the electron density drops below the doping concentration at the anode, the field is reastablished on the anode side of the plasma. After that the plasma is becoming smaller and less dense and eventually collapses and the electric field is restored. Figure 69 (d) shows the recombination rate. Initially the recombination rate is negative (generation) which is the source of the leakage current. During the transient the recombination rate becomes positive inside the plasma column, and the figures show very clearly that the high carrier densities and the high recombination coincide.

The question arises if this simulation is valid or not, since experimentally the very long charge collection times were not observed. This problem is definitely not two-dimensional. ATLAS assumes that evrything is extended 1 μm in the third dimension, which makes the e-h plasma much larger than it is. A 3D calculation would give a much better solution but it is computationally very expensive. Fortunately, we have two properties of the problem on our side. The e-h hole plasma generated by the ion can be considered cylindrically symmetric and its size is much smaller than the diode's dimensions. Considering a cylindrical diode will not change the electrical properties if we use the correct scaling. We performed the cylindrical calculation modeling half of the diode but instructing ATLAS to consider cylindrical symmetry. The results are similar, the effect is there although it is significatly smaller. Figure 70 compares the current transients for the 2D and 2D cylindrical simulations for both the small and full device. The transient currents in the 2D cylindrical calculations are about an order magnitude shorter than in the 2D simulations and the size of the device has the same effect. Figure 71 shows the same physical quantities as in Figure 69 but for the cylindrical model. It is clear that the e-h plasma pushes out the electric field and there is no much charge collection until the plasma collapses. During this time the recombination rate in the plasma is very high. Since the electric field is modified during this time the Gunn-theorem cannot be really applied. Also, when damage is present the recombination (loss of CCE) can be significantly higher then assumed in the 1D model.

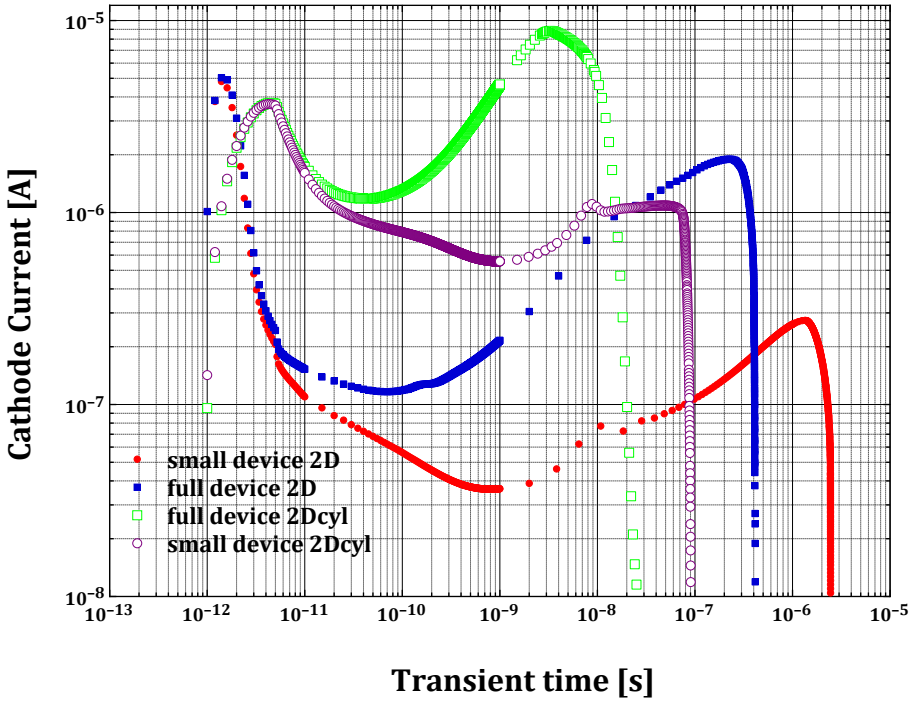

Figure 70 Current transients for 2D and 2D cylindrical models

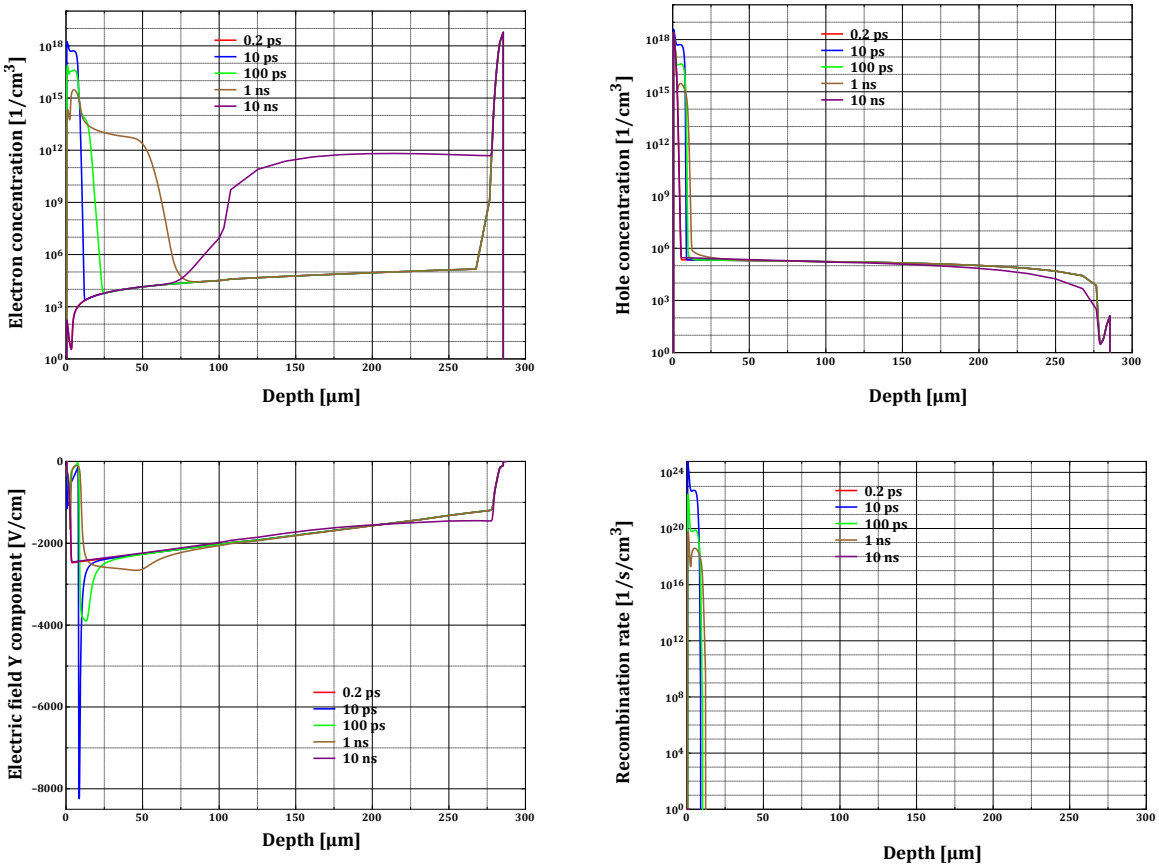

Figure 71 Carrier densities, electric field, and recombination rate during the transient in a 2D cylindrical symmetry

Summary

The following activities were carried out by SNL for the CRP:

- Microbeam and full area irradiation of the Helsinki diodes with various energy H and He beams
- C-V and DLTS analysis of the full area irradiated Helsinki diodes
- IBIC analysis of the microbeam irradiated Helsinki diodes
- C-V and IBIC analysis of electron irradiated Helsinki diodes
- Neutron irradiation of the Helsinki diodes
- C-V and IBIC analysis of the neutron irradiated Helsinki diodes
- Neutron irradiation of commercial Hamamatsu PN and PiN diodes
- C-V and IBIC analysis of the neutron irradiated Hamamatsu diodes
- Marlowe and SRIM calculation of ionization and displacement damage profiles for the ion beams used in the irradiations
- Development of a TCAD model for the IBIC measurement in the Helsinki diodes

Unfortunately, due to budget cuts the support for this for this work at SNL completely disappeared in 2014; therefore, we were not able to contribute to the CRP in the last year.

References

[1] M.T. Robinson, I.M. Torrens, Computer simulation of atomic-displacement cascades in solids in the binary-collision approximation, Physical Review B, 9 (1974) 5008.

[2] E. Tuovinen, Processing of radiation hard particle detectors on Czochralski silicon, Department of Micro and Nanosciences, University of Helsinki, Espoo, Finland, 2008.

[3] ASTM, E1854-07 Standard Practice for Ensuring Test Consistency in Neutron-Induced Displacement Damage of Electronic Parts, ASTM Standards, ASTM International (http://www.astm.org), 2007.

[4] E. Bielejec, G. Vizkelethy, N.R. Kolb, D.B. King, B.L. Doyle, Damage Equivalence of Heavy Ions in Silicon Bipolar Transistors, IEEE Transaction on Nuclear Science, 53 (2006) 3681-3686.

[5] Z. Pastuovic, Progress report of ANSTO for IAEA CRP F11016, International Atomic Energy Agency, 2014.

[6] G. Vizkelethy, Annual report of Sandia National Laboratories (SNL) contribu-tion to IAEA CRP F11016 on "Utilization of ion accelerators for studying and modeling of radiation induced defects in semicon-ductors and insulators", International Atomic Energy Agency, 2013.

[7] R.M. Fleming, C.H. Seager, D.V. Lang, E. Bielejec, J.M. Campbell, Defect-driven gain bistability in neutron damaged, silicon bipolar transistors, Applied Physics Letters, 90 (2007) 172105.

[8] E. Bielejec, G. Vizkelethy, R.M. Fleming, D.B. King, Metrics for Comparison Between Displacement Damage due to Ion Beam and Neutron Irradiation in Silicon BJTs, IEEE Transactions on Nuclear Science, 54 (2007) 2282-2287.
[9] E. Bielejec, G. Vizkelethy, R.M. Fleming, W.R. Wampler, S.A. Myers, D.B. King, Comparison Between Experimental and Simulation Results for Ion Beam and Neutron Irradiations in Silicon Bipolar Junction Transistors, IEEE Transactions on Nuclear Science, 55 (2008) 3055-3059.
[10] E. Bielejec, G. Vizkelethy, N.R. Kolb, D.B. King, B.L. Doyle, Damage equivalence of heavy ions in silicon bipolar junction transistors, IEEE Transactions on Nuclear Science, 53 (2006) 3681-3686.
[11] M. Hou, Linear collision sequences in fcc and Ll(2) metals: A computer simulation study, Nucl. Instrum. Methods Phys. Res. Sect. B-Beam Interact. Mater. Atoms, 187 (2002) 20-35.
[12] R.C. Fletcher, W.L. Brown, Annealing of bombardment damage in a diamond-type lattice - Theoretical, Physical Review, 92 (1953) 585-590.
[13] M. Hou, C.J. Ortiz, C.S. Becquart, C. Domain, U. Sarkar, A. Debacker, Microstructure evolution of irradiated tungsten: Crystal effects in He and H implantation as modelled in the Binary Collision Approximation, J. Nucl. Mater., 403 (2010) 89-100.
[14] M. Jaraiz, J. Arias, L.A. Bailon, J.J. Barbolla, Detailed computer-simulation of damage accumulation in ion irradiated crystalline targets, Vacuum, 44 (1993) 321-323.
[15] K.M. Klein, C.H. Park, A.F. Tasch, Modeling of commulative damage effects on ion-implantation profiles, Nucl. Instrum. Methods Phys. Res. Sect. B-Beam Interact. Mater. Atoms, 59 (1991) 60-64.
[16] A. Scholz, C. Lehmann, Stability Problems, Low-Energy-Recoil Events, and Vibrational Behavior of Point Defects in Metals, Physical Review B, 6 (1972) 813-826.
[17] A. Souidi, M. Hou, C.S. Becquart, C. Domain, Atomic displacement cascade distributions in iron, J. Nucl. Mater., 295 (2001) 179-188.
[18] M.T. Robinson, MARLOWE: Computer Simulation of Atomic Collisions in Crystalline Solids (Version 15b), Radiation Safety Information Computational Center (RSICC), Oak Ridge National Laboratory, Oak Ridge, TN, 2002.
[19] M.T. Robinson, Binding energy effects in cascade evolution and sputtering, Nucl. Instrum. Methods Phys. Res. Sect. B-Beam Interact. Mater. Atoms, 115 (1996) 549-553.
[20] G. Vizkelethy, S.M. Foiles, Determination of recombination radius in Si for binary collision approximation codes, Nuclear Instruments and Methods in Physics Research Section B: Beam Interactions with Materials and Atoms, 371 (2016) 111-115.
[21] ATLAS User's Manual, Silvaco, Inc., 2013.
[22] S. Rath, Progress report of University of New Delhi for IAEA CRP F11016, International Atomic Energy Agency, 2014.
[23] E. Vittone, Electrostatic model of the n-type diode N. 26 from Helsinki Institute of physics, International Atomic Energy Agency, 2012.
[24] J.F. Ziegler, SRIM, http://www.srim.org, 2008.

[25] J.B. Gunn, A General Expression for Electrostatic Induction and its Application to Semiconductor Devices, Solid-State Electronics, 7 (1964) 739-742.